Cell

Article

Activation of the helper NRC4 immune receptor forms a hexameric resistosome

Graphical abstract

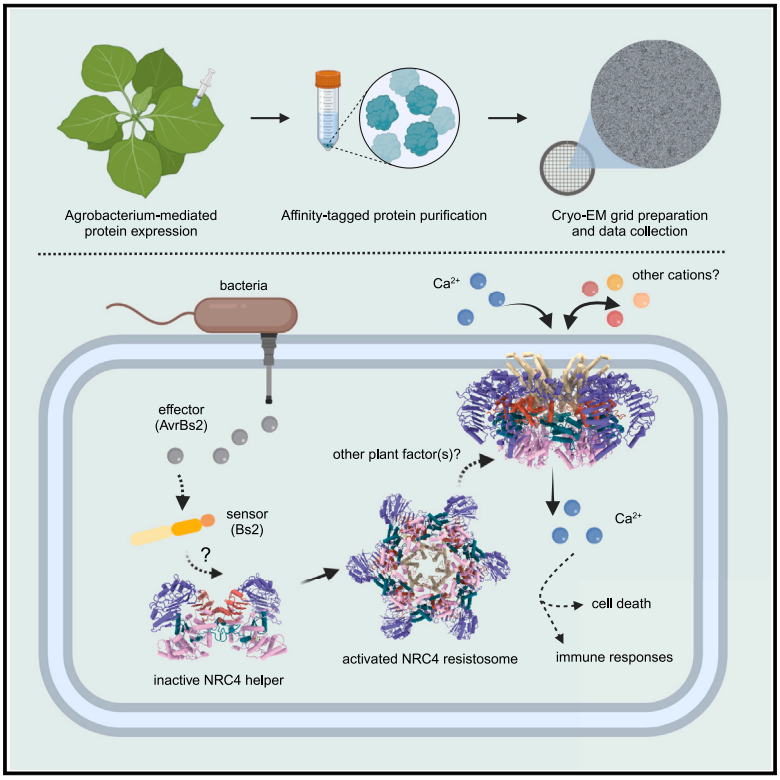

Highlights

- NRC0, NRC2, NRC3, and NRC4 form hexameric resistosomes upon activation
- NRC4 and NRC3 resistosomes trigger calcium influx and immune responses in plants
- NRC activation requires plant-specific factor(s) for calcium influx

Authors

Furong Liu, Zhenlin Yang, Chao Wang, ..., Sheng Luan, Eva Nogales, Brian J. Staskawicz

Correspondence

zhenlinyang@berkeley.edu (Z.Y.), stask@berkeley.edu (B.J.S.)

In brief

The plant helper NRC4 immune receptor forms a hexameric resistosome upon activation, triggering calcium influx and immune responses.

Liu et al., 2024, Cell *187*, 1–13
September 5, 2024
https://doi.org/10.1016/j.cell.2024.07.013

CellPress

Please cite this article in press as: Liu et al., Activation of the helper NRC4 immune receptor forms a hexameric resistosome, Cell (2024), https://doi.org/10.1016/j.cell.2024.07.013

Cell

CellPress

Article

Activation of the helper NRC4 immune receptor forms a hexameric resistosome

Furong Liu,[1,2,10] Zhenlin Yang,[3,4,10,*] Chao Wang,[1] Zhang You,[1] Raoul Martin,[2] Wenjie Qiao,[5] Jian Huang,[6] Pierre Jacob,[7] Jeffery L. Dangl,[7] Jan E. Carette,[5] Sheng Luan,[1] Eva Nogales,[3,4,8,9] and Brian J. Staskawicz[1,2,11,*]

[1]Department of Plant and Microbial Biology, University of California, Berkeley, Berkeley, CA, USA
[2]Innovative Genomics Institute, University of California, Berkeley, Berkeley, CA, USA
[3]California Institute for Quantitative Biosciences (QB3), University of California, Berkeley, Berkeley, CA, USA
[4]Howard Hughes Medical Institute, University of California, Berkeley, Berkeley, CA, USA
[5]Department of Microbiology and Immunology, Stanford University School of Medicine, Stanford, CA, USA
[6]Department of Molecular Biology, Princeton University, Princeton, NJ, USA
[7]Department of Biology and Howard Hughes Medical Institute, University of North Carolina at Chapel Hill, Chapel Hill, NC 27599, USA
[8]Department of Molecular and Cell Biology, University of California, Berkeley, Berkeley, CA, USA
[9]Molecular Biophysics and Integrative Bioimaging Division, Lawrence Berkeley National Laboratory, Berkeley, CA, USA
[10]These authors contributed equally
[11]Lead contact
*Correspondence: zhenlinyang@berkeley.edu (Z.Y.), stask@berkeley.edu (B.J.S.)
https://doi.org/10.1016/j.cell.2024.07.013

SUMMARY

Innate immune responses to microbial pathogens are regulated by intracellular receptors known as nucleotide-binding leucine-rich repeat receptors (NLRs) in both the plant and animal kingdoms. Across plant innate immune systems, "helper" NLRs (hNLRs) work in coordination with "sensor" NLRs (sNLRs) to modulate disease resistance signaling pathways. Activation mechanisms of hNLRs based on structures are unknown. Our research reveals that the hNLR, known as NLR required for cell death 4 (NRC4), assembles into a hexameric resistosome upon activation by the sNLR Bs2 and the pathogenic effector AvrBs2. This conformational change triggers immune responses by facilitating the influx of calcium ions (Ca^{2+}) into the cytosol. The activation mimic alleles of NRC2, NRC3, or NRC4 alone did not induce Ca^{2+} influx and cell death in animal cells, suggesting that unknown plant-specific factors regulate NRCs' activation in plants. These findings significantly advance our understanding of the regulatory mechanisms governing plant immune responses.

INTRODUCTION

Plants and animals rely on innate immune receptors to detect and respond to invading pathogens. In plants, these receptors are primarily of two types: cell-surface pattern recognition receptors (PRRs) and intracellular nucleotide-binding leucine-rich repeat receptors (NLRs).[1–4] PRRs recognize microbe- or pathogen-associated molecular patterns and activate pattern-triggered immunity (PTI), while NLRs detect pathogen effectors either directly or indirectly by recognizing alterations of host targets, ultimately leading to the activation of effector-triggered immunity (ETI).[1–4] Recent research has unveiled an intricate interplay between ETI and PTI in plants.[5–10] It has been revealed that NLRs not only execute their direct roles in ETI but also significantly contribute to the enhancement of PTI by upregulating PTI signaling components.[5–10]

Recognition of pathogen effectors leads to the oligomerization of NLRs.[11–15] For example, recognition of the pathogen effectors XopQ1 and ATR1 by Toll/interleukin 1 receptor (TIR) domain-containing NLR (TNL)-type resistance proteins ROQ1 and RPP1 leads to the formation of tetrameric resistosomes.[12,13] These tetramers activate the nicotinamide adenine dinucleotide nucleosidase (NADase) activity of the TIR domain, generating small molecules that serve as second messengers to activate downstream immune responses.[16–21] On the other hand, *Arabidopsis* HOPZ-ACTIVATED RESISTANCE 1 (ZAR1) and wheat stem rust resistance 35 (Sr35) form pentameric resistosomes upon effector detection.[11,14,15] The N-terminal coiled-coil (CC) domains of these resistosomes insert into the plasma membrane (PM), forming calcium (Ca^{2+}) permeable cation channels, resulting in robust Ca^{2+} influx across the PM and elevation in cytosolic Ca^{2+} ($[Ca^{2+}]_{cyt}$), essential for inducing defense responses and cell death.[14,22]

Specific NLRs, referred to as helper NLRs (hNLRs), are essential for collaborating with and facilitating certain sensor NLRs (sNLRs) to regulate PTI and ETI responses.[23–27] NLRs required for cell deaths (NRCs) are well-known hNLRs in *Solanaceous* plants that transmit immune signals from various sNLRs and

Please cite this article in press as: Liu et al., Activation of the helper NRC4 immune receptor forms a hexameric resistosome, Cell (2024), https://doi.org/10.1016/j.cell.2024.07.013

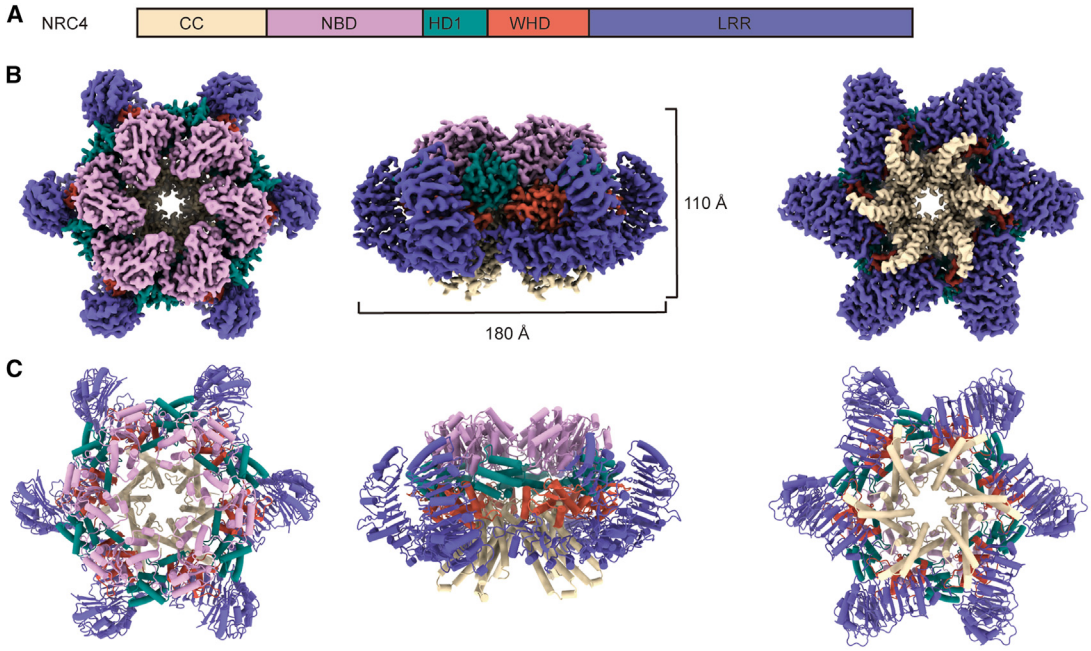

Figure 1. Structure of the NRC4 resistosome

(A) Domain organization of NRC4. The same color code for the domains is used throughout this study, unless specified otherwise.

(B) Cryo-EM density map of the hexameric NRC4 structure.

(C) The corresponding refined structure model (top, side, and bottom views are shown from left to right). Six identical NRC4 protomers are arranged in a wheel-like structure measuring ~180 Å in diameter and 100 Å in height.

See also Figures S1–S3 and Table 1.

specific PRRs.[9,25] NRC2, NRC3, and NRC4 have been implicated in effector recognition and the assembly of macromolecular complexes.[26,27] Subsequently, these oligomers initiate ETI, resulting in a programmed cell death known as the hypersensitive response (HR) associated with the limitation of pathogen proliferation.[2] A specialized class of hNLRs, known as resistance to powdery mildew 8 (RPW8)-like CC domain NLRs (RNLs), exists to transduce TIR-dependent small molecule signals to immune responses. These RNLs, N REQUIRED GENE1 (NRG1), and ACTIVATED DISEASE RESISTANCE1 (ADR1) oligomerize and form Ca^{2+}-permeable cation channels, leading to an increase in $[Ca^{2+}]_{cyt}$ levels and cell death.[28] However, it is unknown whether the activation of NRCs directly or indirectly results in Ca^{2+} influx.

Recent cryoelectron microscopy (cryo-EM) studies provide valuable insights into the structures of sNLR resistosomes.[11–15] However, the structures of activated hNLRs are still unknown, limiting our understanding of the molecular basis, activation, and regulation of these indispensable components in plant immune responses.

RESULTS

Reconstitution and cryo-EM structure of the active NRC4 resistosome

sNLRs are known to trigger the oligomerization of associated hNLRs upon detecting effectors from plant pathogens.[10,26,27] The L9E mutation of NRC4 abolishes HR cell death activity induced by the active NRC4.[29] Our data demonstrate that recognition of the bacterial effector AvrBs2 by sNLR Bs2 induces NRC4 L9E to form a hexameric resistosome, as observed by negative staining EM (Figures S1A and S1B). To stabilize the NRC4 resistosome for isolation from *Nicotiana benthamiana* (*N. benthamiana*) leaves, we introduced two mutations into NRC4. The D478V (DV) mutation within the methionine-histidine-aspartate (MHD) motif is an activation mimic mutation favoring ATP binding over ADP.[30–32] Additionally, as noted above, the L9E mutation suppresses HR cell death induced by NRC4 DV[29] (Figures S1C and S1D), enabling stabilization and isolation of the active NRC4 resistosome without causing cell death. Co-inoculation of *N. benthamiana* leaves with vectors carrying either a 3× FLAG or a Twin-StrepTag II, along with NRC4 with the two mutations, resulted in efficient tandem affinity purification of the NRC4 protein with high purity (Figure S1E). The NRC4 protein follows the typical CNL domain structure, with an N-terminal CC domain, a nucleotide-binding domain (NBD), helical domain 1 (HD1), a winged-helix domain (WHD), and a C-terminal leucine-rich-repeat (LRR) domain[29] (Figure 1A). Cryo-EM grids, supported by either carbon or graphene layers, were used to concentrate the resistosome for detailed visualization. Further cryo-EM data analysis yielded a 2.6 Å resolution structure of the hexameric NRC4 resistosome (Figures 1B, 1C, S2, S3A–S3D, and S4; Table 1).

Overall structure of NRC4 resistosome

The resolution of the cryo-EM maps allowed us to use *de novo* atomic models to build NRC4 oligomers, which exhibit architectural features akin to well-established pentameric CNL

Please cite this article in press as: Liu et al., Activation of the helper NRC4 immune receptor forms a hexameric resistosome, Cell (2024), https://doi.org/10.1016/j.cell.2024.07.013

structures.[11,14,15] The hexameric assembly of NRC4 results in a wheel-like structure measuring approximately 180 Å in diameter and 100 Å in height (Figure 1B). Compared with that of the ZAR1 and Sr35 CNL resistosomes, the organization of the NRC4 hexamer involves a more densely packed arrangement of protomers (Figures 1B, 1C, and S1F). This dense packing, particularly of the LRR domain, potentially limits the available space for interactions with external protein factors, as observed for effectors in the case of ZAR1 and Sr35.[11,14,15] The LRR domain in NRC4 arranges at a smaller angle relative to the tangent of the wheel-like structure, allowing the LRR to extend more prominently into the solvent and thus compensating for the restricted space between adjacent LRRs (Figures 1B and 1C). Structural comparison of the LRR domains of NRC4 with Sr35 and ZAR1 reveals similar overall structures, with root-mean-square deviation (RMSD) of 1.022 and 1.055, respectively (Figure S1G). However, electrostatic surface analysis of these LRR domains highlights distinct features. Notably, NRC4 exhibits a more positively charged surface (Figure S1H), suggesting that NRC4 may utilize a different mechanism to interact with its protein partners compared with Sr35 and ZAR1. In the hexameric NRC4 resistosome, the α1 helix in the CC domain, equivalent to that of Sr35,[14] was not visible, likely due to flexibility. By contrast, in the ZAR1 resistosome structure, the α1 helices from five protomers were found to form a funnel-shaped structure, locating the resistosome to the membrane.[11]

Oligomerization of the NRC4 resistosome

Protomer packing in the NRC4 resistosome structure is governed by multiple interactions involving the five domains (Figure 2A). In the interaction between adjacent CC domains, the α2-helix from one protomer engages with the α3-helix of its neighboring protomer (Figure 2B). D47 from α2-helix forms hydrogen bonds with the main chain of E56 and Q57 in the α3-helix (Figure 2B), and Q129 from the α2-helix forms hydrogen bonds with the main chain of Q126 in the α3-helix (Figure 2B). Interestingly, NBD-NBD interaction, previously implicated in protomer packing and contributing to Sr35 and ZAR1 resistosome formation,[11,14] was not detected in the NRC4 structure. Instead, we observed that amino acids E283 and D275 from the NBD domain form two salt bridge interactions with K329 and R362, respectively, in the HD1 domain of the neighboring protomer (Figure 2C). D453 from the WHD is also engaged in a salt bridge interaction with R364 from the HD1 domain (Figure 2D). Similar to ZAR1, but unlike Sr35, the LRR domains pack directly against each other, with a hydrogen bond between C661 and D502 (Figure 2E).[11,14]

To assess the significance of these interactions in facilitating the NRC4 DV-mediated HR cell death, we introduced single-point mutations and group mutations at these interfaces. Two group mutations, H40A/D47A/Q129A and D275A/E283A/D453A, completely abolished cell death activity (Figure 2G). Notably, the single mutation D47A was capable of abolishing cell death in *N. benthamiana* leaves, highlighting the importance of this residue in NRC4 function (Figure 2G). Both wild-type NRC4 and all tested mutants that hinder HR exhibited comparable protein levels, indicating that these substitutions do not affect NRC4 stability (Figure 2H).

ATP binding leads to a sequence of structural rearrangements crucial for NLRs to switch from inactive to active states.[11,14] Our NRC4 structure shows clear density for an ATP molecule located within the cleft formed by the NBD and HD1 domains (Figure 2F). This position resembles that seen for Sr35 but differs from the configuration in the ZAR1 resistosome, where ATP predominantly interacts with the WHD domain.[11,14,15] In NRC4, ATP only interacts with residues in the NBD, despite its proximity to the HD1 domain (Figure 2F). Specifically, T192 hydrogen bonds with the adenine base of ATP, while K190, T191, and R295 interact with the ATP phosphates (Figure 2F). Mutations disrupting these interactions (K190A/T191A/T192A/R295A) led to the inhibition of HR in *N. benthamiana* leaves (Figure 2G). A significant loss of HR was also observed with the single-point mutation T191A (Figure 2G), emphasizing its essential role in ATP binding. Importantly, the protein levels of wild-type NRC4 and all tested mutants that hinder HR remained comparable, indicating that these substitutions do not affect the stability of NRC4 and do not prevent NRC4 from oligomerizing upon activation (Figures 2H and S3I).

Conservation of the EDVID motif and LRR$^{R\text{-}cluster}$ in NRC4

The EDVID (Glu-Asp-Val-IIE-Asp) sequence motif in the α3-helix is engaged with a positively charged region on the LRR domains known as the R-cluster motif, resulting in intramolecular interactions that have been shown to be critical for CNL-mediated cell death.[14,33] In the NRC4 resistosome structure, only this α3-helix interacts with the LRR domain, while the other helices within the CC domain do not participate in such interaction (Figure 3A). Residues E73, D74, and D77 within the α3-helix form salt bridges and hydrogen bonds with R514 and R537 of the LRR domain (Figure 3B). Electrostatic surface analysis of the LRR domain in NRC4 revealed a striking similarity in size to the R-cluster observed in ZAR1 and Sr35 (Figure 3C). Sequence alignment analysis further revealed the conservation of the EDVID motif when comparing NRCs with ZAR1 and Sr35 (Figure 3D). The two arginine residues (R514 and R537) in the R-cluster of NRC4 involved in the interaction with CC domain are also present in Sr35 (Figure 3D). While five arginine residues from distinct repeats within the LRR domain engage in extensive interactions with the CC domain in both of ZAR1 and Sr35 resistosome structures,[11,14] fewer arginines in the NRC4 LRR domain interact with the CC domain (Figures 3B and 3D).

To assess the importance of the EDVID motif and the R-cluster in the immune response, we mutated key amino acids participating in this interaction. We found both triple mutations of E73A/D74A/D77A in the EDVID motif and double mutations of R514A/R537A in the R-cluster resulted in a loss of cell death activity (Figure 3E), without affecting the stability of NRC4 protein (Figure 3F). Single amino acid substitutions of E73, D74, or D77 failed to abolish cell death activity (Figure 3E), while the single R514A or R537A substitution was enough to hinder cell death activity (Figure 3F), emphasizing the crucial role of these two arginines within the R-cluster (Figures 3B and 3D). Additionally, these mutations did not prevent NRC4 from oligomerizing

Please cite this article in press as: Liu et al., Activation of the helper NRC4 immune receptor forms a hexameric resistosome, Cell (2024), https://doi.org/10.1016/j.cell.2024.07.013

Table 1. Statistics of the cryo-EM data collection, processing, and refinement

Data collection and processing	NRC4 hexamer (PDB: 9CC8 EMDB:EMD-45437)	NRC4 dodecamer (PDB: 9CC9 EMDB: EMD-45438)
Microscope	Krios	Krios
Camera	K3	K3
Voltage (kV)	300	300
Camera magnification	81,000	81,000
Pixel size (Å)	1.05	1.05
Electron exposure (e^{-}/Å^2)	50	50
Number of frames per exposure	50	50
Defocus range (μm)	−1 ∼ −2	−1 ∼ −2
Automation software	SerialEM	SerialEM
Micrographs collected (no.)	27,770	27,770
Refined particles (no.)	80,368	28,066
Map resolution (Å)	2.64	3.54
Map resolution range (Å)	2.2–3.8	3.0–5.0
Sharpening tool	cryoSPARC	cryoSPARC
Map sharpening B factor (Å^2)	88.7	95.4
Model composition		
Ligand	6	12
Protein	6	12
Residues	5,028	10,194
Refinement		
Refinement package	phenix	phenix
Real or reciprocal space	real	real
Resolution cutoff (Å)	2.64	3.54
Model-Map scores		
CC	0.74	0.65
FSC 0.5 (Å)	2.9	4.1
B factors (Å^2)	67.99	117.85
RMSD		
Bond length (Å)	0.005	0.006
Bond angles (°)	0.648	0.760
Validation		
MolProbity score	1.99	2.2
CaBLAM outliers	1.78	2.61
Clash score	6.94	19.67
Ramachandran plot		
Favored (%)	95.49	93.82
Allowed (%)	4.23	5.92
Outliers (%)	0.28	0.26

upon activation (Figure S3I). These findings suggest an essential involvement of the EDVID and R-cluster motifs in NRC4 DV-mediated cell death.

An NRC4 activation mimic triggers Ca^{2+} influx in planta

Increasing evidence underscores the critical role of Ca^{2+} signaling in the initiation of ETI.[34–37] Particularly relevant are the findings that activated CNLs (e.g., ZAR1 and Sr35) and hNLRs (e.g., NRG1.1) assemble into pore-forming resistosomes within the PM, facilitating the influx of extracellular Ca^{2+} into the cytosol.[14,22,28] We thus hypothesized that the activation of NRC4 may trigger a Ca^{2+} influx that appears to be a common downstream event of NLR activation. To test this hypothesis, we transiently expressed several NRC4 variants, including the activation mimic NRC4 DV, in *N. benthamiana* leaves expressing the $[Ca^{2+}]_{cyt}$ reporter GCaMP3.[38] Our results revealed a strong $[Ca^{2+}]_{cyt}$ increase approximately 8–9 h after leaf infiltration with *Agrobacterium* carrying vectors expressing the activation mimic NRC4 DV (Figures 4A and 4B). Notably, this $[Ca^{2+}]_{cyt}$ increase preceded the onset of leaf HR cell death, which typically occurred over an extended time frame (Figure S1C). By contrast, the wild-type NRC4, or the variants NRC4 L9E and NRC4 L9EDV, failed to induce either $[Ca^{2+}]_{cyt}$ increase (Figures 4A and 4B) or cell death (Figure S1C). Similarly, activation mimics NRC3 D480V (NRC3 DV), and NRG1.1 D485V (NRG1.1 DV) also induced Ca^{2+} influx (Figures 4C and 4D), consistent with the previous report.[28]

Furthermore, application of a Ca^{2+}-channel blocker, lanthanum (III) chloride ($LaCl_3$), effectively abolished NRC4 DV-mediated $[Ca^{2+}]_{cyt}$ increase (Figures 4E and 4F) and HR cell death (Figure S5A). We also assessed other chemical inhibitors, including tetraethylammonium chloride (TEACl) and cesium chloride (CsCl), as well as an intracellular Ca^{2+} release blocker, ruthenium red (RR). All these inhibitors appeared to not notably inhibit the NRC4 DV-mediated $[Ca^{2+}]_{cyt}$ increase as seen in $LaCl_3$ treated leaves (Figures 4G and 4H), suggesting a specific Ca^{2+} entry through the PM from the extracellular space. Consistent with these observations, elevated external Ca^{2+} enhanced NRC4 DV-mediated Ca^{2+} influx (Figures 4I and 4J).

We attempted to assess the Ca^{2+} channel activity of NRC4 DV in human embryonic kidney (HEK) 293 cells.[28] We loaded Fura-2 Ca^{2+} indicator into HEK293 cells expressing the activation mimic NRC4 DV or NRG1.1 DV. Cells were incubated with a low Ca^{2+} buffer, followed by an extracellular Ca^{2+} treatment. Interestingly, NRC4 DV-expressing cells did not express $[Ca^{2+}]_{cyt}$ elevation (Figure S5G), unlike NRG1.1 DV-expressing cells that displayed Ca^{2+}-induced $[Ca^{2+}]_{cyt}$ elevation.[28] It appeared that NRC4 DV was not associated with PM in HEK293 cells, which may explain the lack of $[Ca^{2+}]_{cyt}$ increase and subsequent cell growth defects in the NRC4 DV-expressing cells (Figures S5D–S5F). Like NRC4 DV, the activation mimics NRC2 H480R (NRC2 HR), and NRC3 DV did not induce growth defects in the HEK293 cells either, implicating a conserved mechanism across NRC family hNLRs (Figures S5D and S5E).

Please cite this article in press as: Liu et al., Activation of the helper NRC4 immune receptor forms a hexameric resistosome, Cell (2024), https://doi.org/10.1016/j.cell.2024.07.013

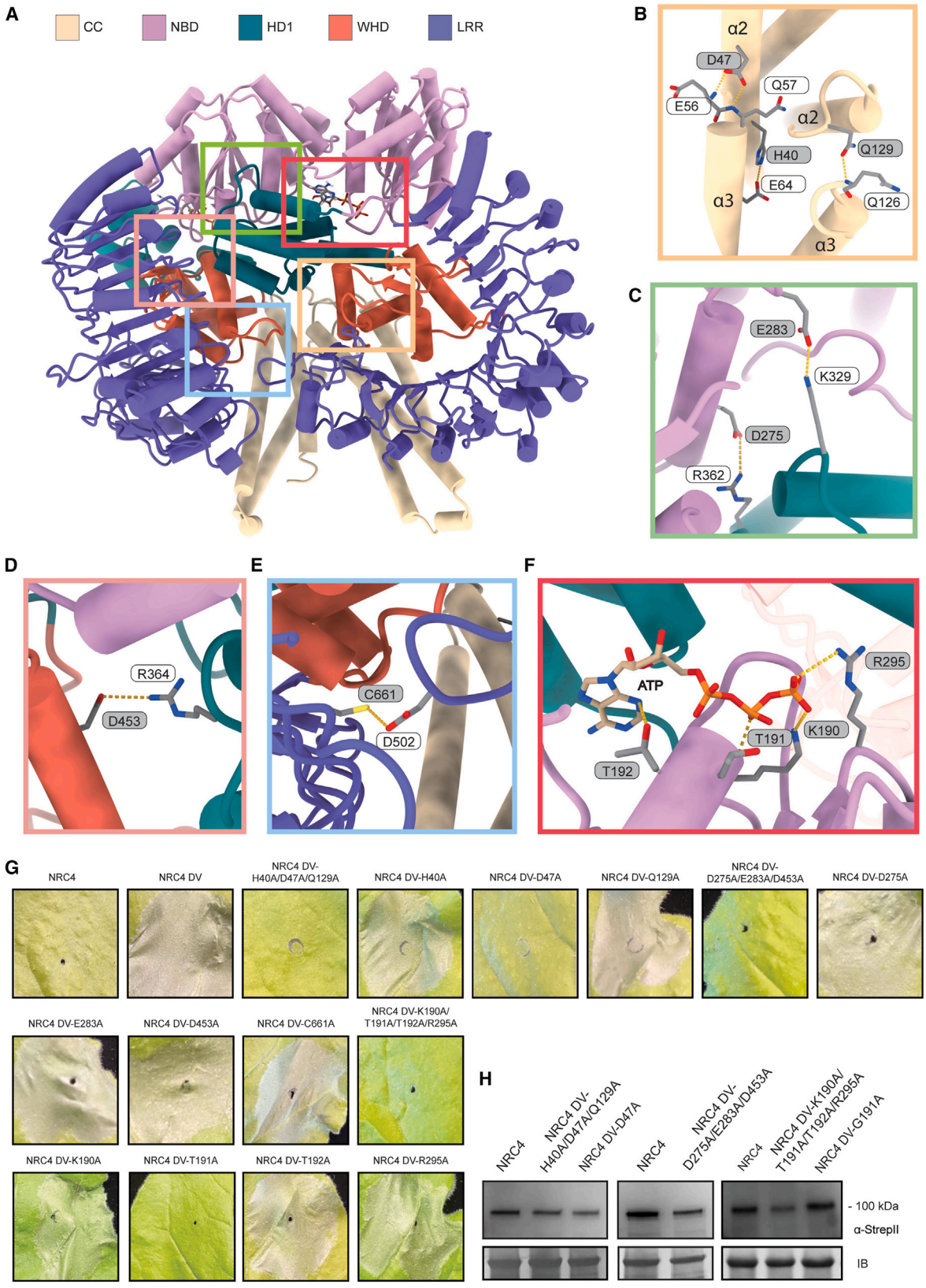

(legend on next page)

Please cite this article in press as: Liu et al., Activation of the helper NRC4 immune receptor forms a hexameric resistosome, Cell (2024), https://doi.org/10.1016/j.cell.2024.07.013

In addition, we used *Xenopus* oocytes to evaluate NRC4 resistosome-mediated cell death and its potential Ca^{2+} channel activity. Consistent with the results in HEK293 cells (Figures S5E and S5F), NRG1.1 DV induced strong cell death in *Xenopus* oocytes. By contrast, NRC4 DV alone or NRC4 in combination with the effector/sensor (AvrBs2/Bs2) did not (Figure S5H). Using two electrode voltage-clamp (TEVC) recording, we recorded a strong Ca^{2+} conductance in the living oocytes expressing NRG1.1 DV group but not the oocytes expressing NRC4 DV (Figures S5I–S5K). Taken together, these results indicate that NRC resistosomes evolved a distinct activation mechanism, requiring unknown plant factors for effective function in heterologous expression systems. This differs from the other previously reported CNL or RNL plant resistosomes.[14,22,28]

Structurally, the NRC4 resistosome exhibits a hexameric architecture, while both Sr35 and ZAR1 are pentamers.[11,14,15] Within the NRC4 resistosome, the putative ion-conducting pore is partitioned into a central cavity and an intracellular cavity, with a pronounced constriction site near Gln126 (Figure 5A). NRC4 and Sr35 shared a similarly dilated constriction site compared with ZAR1, albeit with a tighter constriction. Despite the absence of a resolved N terminus analogous to the α1 helix in NRC4 and Sr35 in EM densities, all three resistosomes display a comparable size of central cavity adjacent to the constriction site. Notably, a significant disparity is observed in the NRC4 resistosome, featuring a larger intracellular cavity than those in Sr35 and ZAR1 (Figures 5B and 5C). Together, these results support the conclusion that the active NRC4 resistosome facilitates the influx of extracellular Ca^{2+} into the cytosol of plant cells in combination with other plant factor(s) as a pivotal prerequisite for NRC4 resistosome-mediated HR cell death. The detailed mechanisms underlying PM association and Ca^{2+} influx require future research.

DISCUSSION

Distinct activation mechanisms of sNLR-hNLR pairs in mammals and plants

In mammalian cells, the NLR family of apoptosis inhibitory proteins (NAIPs) act as sNLRs and are activated by binding to specific bacterial protein ligands.[40] Upon activation, NAIPs co-assemble with a downstream hNLR, the NLR family caspase activation and recruitment domain (CARD) domain-containing protein 4 (NLRC4), forming NAIP-NLRC4 inflammasomes, which play crucial roles in the innate immune system.[41–43] Each inflammasome comprises one NAIP and multiple NLRC4 protomers.[40,43] Our study shows that the activation mimic NRC4 DV oligomerizes without the need to incorporate the corresponding effector-activated sNLRs. The presence of six identical protomers in the activation mimic NRC4 DV resistosome and the lack of co-immunoprecipitation with effector-activated Bs2 sNLR (Figure S1B) support an activation-and-release model for plant sNLR/hNLR signaling.[26,27] A similar result was observed in recent work, showing NRC3 only forms transient binding with sNLR.[44] These results indicate that hNLRs do not form a stable complex with sNLRs.[26,27] Thus, our findings highlight the differences in the activation mechanisms of sNLR/hNLR pairs between plants and animals.

Structural analyses of NLR proteins provide mechanistic insights into the plant immune response

The evolutionary arms race between plants and pathogens has driven an increase in NLR complexity. Ancestral multifunctional NLRs evolved into specialized receptors with distinct sensor and helper roles, followed by further functional diversification.[45,46] In all NLR catalogs, certain CNLs like ZAR1 sense effectors and trigger immune responses and retain their conserved ancestral structure and functional roles across plant species.[11] However, many other NLRs form pairs and functionally redundant networks (NRCs), with sensors and helpers facilitating signaling and cell death, introducing more complex regulatory mechanisms.[46] In the past 5 years, structural approaches, particularly cryo-EM, have uncovered molecular mechanisms of plant CNL and TNL protein activation. The structures of tetrameric and pentameric singleton resistosomes from *Arabidopsis* and wheat significantly broadened our understanding of key components in plant immunity.[11–15] Our study revealed the structure of the hexameric activated helper NRC4 resistosome from *N. benthamiana*, expanding the scope of NLR resistosome structural variation. Considering the complex regulatory mechanisms of NLR proteins, including the paired NLRs or NLRs in conjunction with other NLRs that suppress the immune responses, additional structural studies are likely to add additional structural variation and define additional modes of immune response activation.

α1 helices in ZAR1, Sr35, and NRC4: Roles in plant immunity

In the ZAR1 structure, the first alpha-helices form a funnel-shaped structure to anchor the resistosome to the membrane.[22] However, in the activated NRC4 resistosome structure, the first α1 helix is not visible, nor is it visible in the Sr35 resistosome, likely due to intrinsic flexibility. This similarity indicates that NRC4 and Sr35 likely have a similar interaction pattern with the membrane. A previous study demonstrated that the ZAR1 α1 helix can functionally replace the NRC4 α1 helix, allowing the

Figure 2. Interfaces in the oligomerization of the NRC4 resistosome

(A) View of two adjacent protomers in the NRC4 resistosome. Boxes indicate regions of interaction between them, shown in detail in (B)–(F).

(B–E) Structural details of CC-CC, NBD-HD, WHD-HD1, and LRR-LRR interactions, respectively. Residue labels in both gray and white correspond to two adjacent protomers.

(F) ATP is situated in the cleft between the NBD and HD1 domain, interacting exclusively with the NBD despite its proximity to both domains.

(G) Hypersensitive response phenotypes of *N. benthamiana* leaves upon the expression of mutant NRC4 proteins based on the interfaces shown in (B)–(F). A representative figure from multiple replicates is shown for each case.

(H) Protein expression levels of the wild-type NRC4 and the tested mutants in the *N. benthamiana* leaves were evaluated using SDS-PAGE and subsequent immunoblotting with α-StrepTag II antibody. An InstantBlue Coomassie-stained gel was used as a loading control (IB, InstantBlue).

See also Figure S4.

Please cite this article in press as: Liu et al., Activation of the helper NRC4 immune receptor forms a hexameric resistosome, Cell (2024), https://doi.org/10.1016/j.cell.2024.07.013

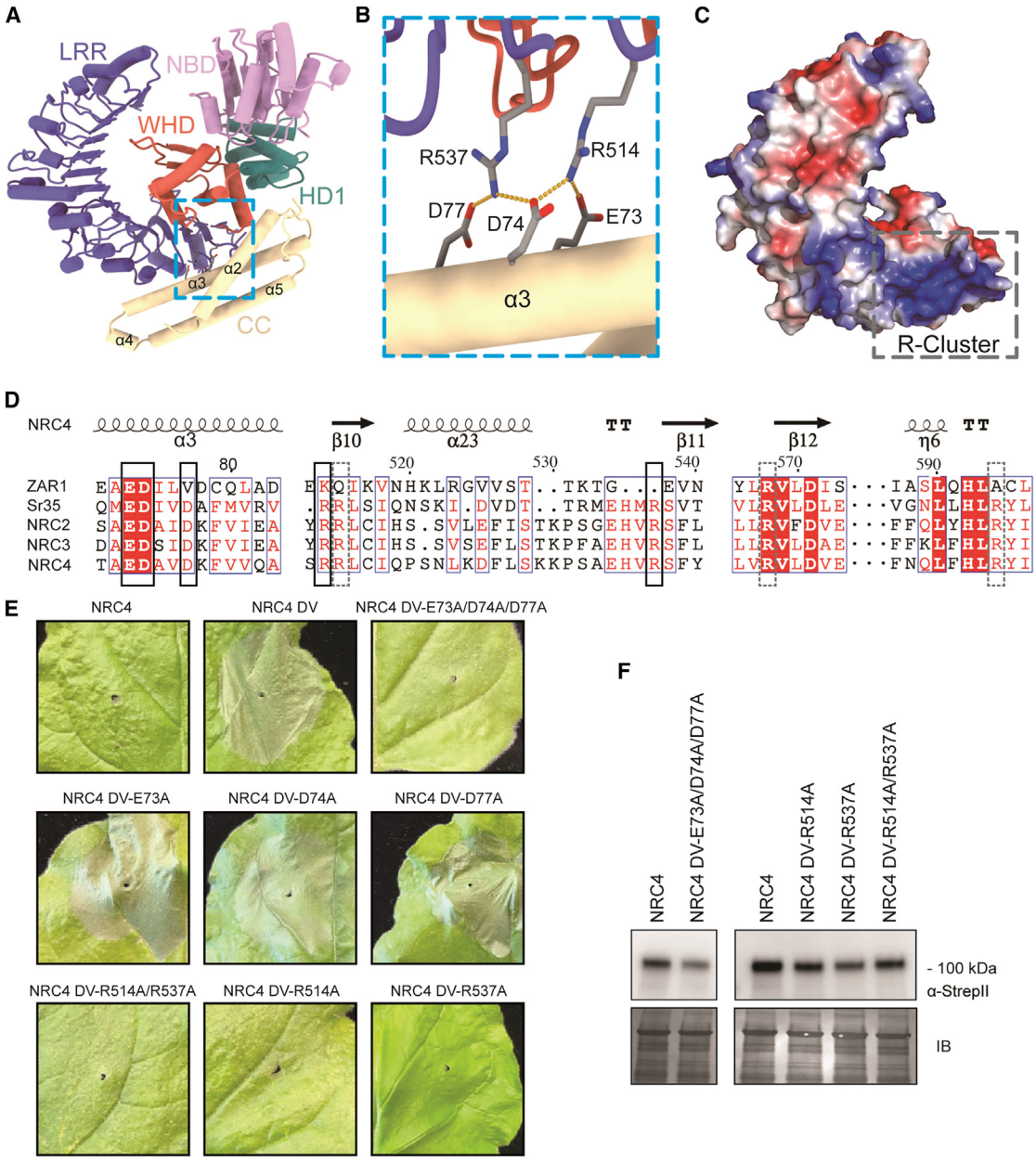

Figure 3. CC-LRR interactions within an NRC4 protomer

(A) Structure of one NRC4 protomer, with the CC-LRR interaction region indicated by a light blue dashed box.

(B) Structural details of the CC-LRR interactions. Three negatively charged residues (E73, D74, and D77) from the CC domain form salt bridges and hydrogen bond interactions with two positively charged residues (R514 and R537) from the LRR domain.

(C) Electrostatic surface view of the LRR domain. The position of the conserved R-cluster is indicated by a dashed box.

(D) Structure-based sequence alignment encompassing the EDVID motif and R-cluster of ZAR1, Sr35, NRC2, NRC3, and NRC4. Key residues from (B) are highlighted by a solid box, while the additional arginines involved in the CC-LRR interaction of the Sr35 resistosome are highlighted by a dashed box.

(E) Hypersensitive response phenotypes of *N. benthamiana* leaves upon the expression of NRC4 with mutations in the residues from (B). In each case, a representative figure is shown from multiple replicates.

(F) Protein expression levels of the wild-type NRC4 and the tested mutants in the *N. benthamiana* leaves were evaluated using SDS-PAGE and subsequent immunoblotting with α-StrepTag II antibody. An InstantBlue Coomassie-stained gel was used as a loading control.

ZAR1$_{1-17}$-NRC4 chimeric protein to trigger cell death in *N. benthamiana* and retain the ability to confer resistance against pathogens.[29] However, critical differences exist, including the existence of non-conserved E11/E18 residues in ZAR1, which affect the funnel's interior space. These are absent in NRC4, implying mechanistic disparities between ZAR1 and NRC4.

Please cite this article in press as: Liu et al., Activation of the helper NRC4 immune receptor forms a hexameric resistosome, Cell (2024), https://doi.org/10.1016/j.cell.2024.07.013

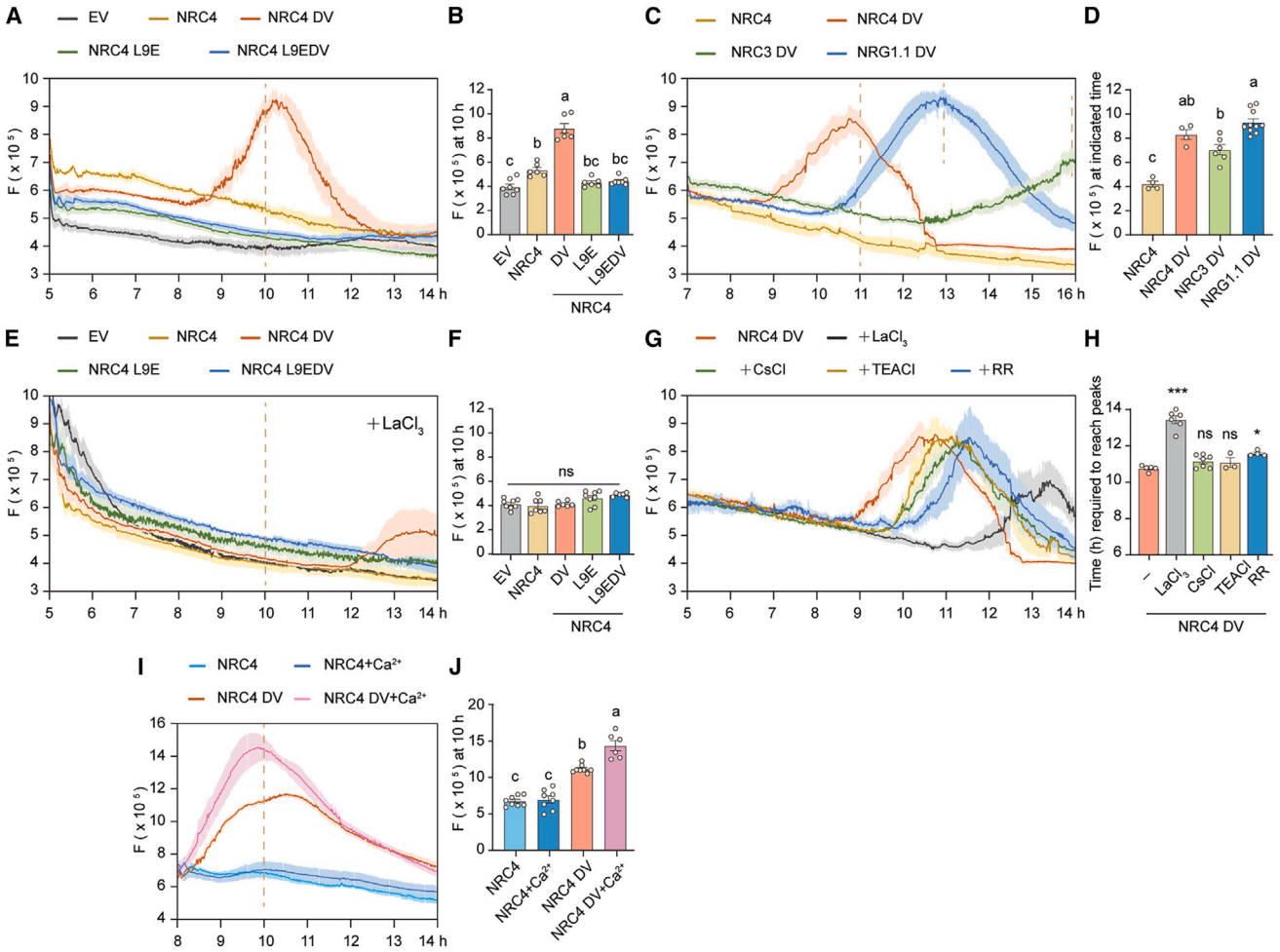

Figure 4. $[Ca^{2+}]_{cyt}$ dynamics upon the expression of NRC4 variants and indicated treatments

(A) Time course of $[Ca^{2+}]_{cyt}$ dynamics after infiltration of *N. benthamiana* leaves expressing the $[Ca^{2+}]_{cyt}$ reporter GCaMP3 with *Agrobacterium* strains carrying the indicated constructs. NRC4 DV and NRC4 L9E denote NRC4 variants with amino acid substitutions D478V and L9E, respectively. NRC4 L9EDV indicates an NRC4 variant with both mutations. Leaf disc fluorescent (F) intensities of GCaMP3, as indicative of relative $[Ca^{2+}]_{cyt}$ levels, are plotted over a tested time. The activation mimic NRC4 DV, unlike other variants, exhibited a robust increase in $[Ca^{2+}]_{cyt}$.

(B) Relative $[Ca^{2+}]_{cyt}$ levels at indicated time as shown in (A).

(C) Time course of $[Ca^{2+}]_{cyt}$ dynamics after expressing indicated constructs. NRG1.1 DV denotes NRG1.1 variant with amino acid substitution D485V, and NRC3 DV denotes variant with amino acid substitution D480V.

(D) Relative $[Ca^{2+}]_{cyt}$ levels at indicated time (NRC4 DV at 11 h, NRG1.1 DV at 13 h, and NRC3 DV at 16 h) as shown in (C).

(E) Time course of $[Ca^{2+}]_{cyt}$ dynamics upon the expression of NRC4 variants co-infiltrated with a PM calcium channel blocker, $LaCl_3$ (2 mM).

(F) Relative $[Ca^{2+}]_{cyt}$ levels at indicated times as shown in (E).

(G) Time course of $[Ca^{2+}]_{cyt}$ dynamics upon the expression of NRC4 DV co-infiltrated with K^+-channel blockers, TEACl (1 mM), and CsCl (1 mM), an intracellular Ca^{2+} release blocker RR (1 mM), or $LaCl_3$ (1 mM).

(H) Time required to reach peaks for the relative $[Ca^{2+}]_{cyt}$ levels as shown in (G).

(I) Time course of $[Ca^{2+}]_{cyt}$ dynamics, showing additive effects of extracellular Ca^{2+} (10 mM) on NRC4 DV-mediated Ca^{2+} influx.

(J) Relative $[Ca^{2+}]_{cyt}$ levels at indicated time as shown in (I). Error bars in (A)(F) represent standard error (n = 6 to 8 discs from 3 independent plants). Experiments were repeated twice with similar phenotypes observed. One-way ANOVA comparison among groups for (B), (D), (F), and (J) or between control with other groups (H), $^{***}p < 0.001$, $^{*}p < 0.05$.

See also Figure S5.

Structural and functional consequences of L9E mutation in NRC4 resistosome formation

The L9E mutation in the α1-helix was introduced to capture the active state of the NRC4 resistosome without causing cell death. In the inactive forms of ZAR1, as well as the predicted inactive forms of Sr35 and NRC4, the α1-helix is buried within the CC bundle and remains unexposed to the solvent.[11] Thus, the L9E mutation is unlikely to impact the interaction between inactive NRC4 and sNLRs. Conversely, in the active state of ZAR1, the α1-helices transform into a funnel that embeds into the membrane, acting as a Ca^{2+} ion channel to initiate an immune response.[22] Although the α1-helix is not

Please cite this article in press as: Liu et al., Activation of the helper NRC4 immune receptor forms a hexameric resistosome, Cell (2024), https://doi.org/10.1016/j.cell.2024.07.013

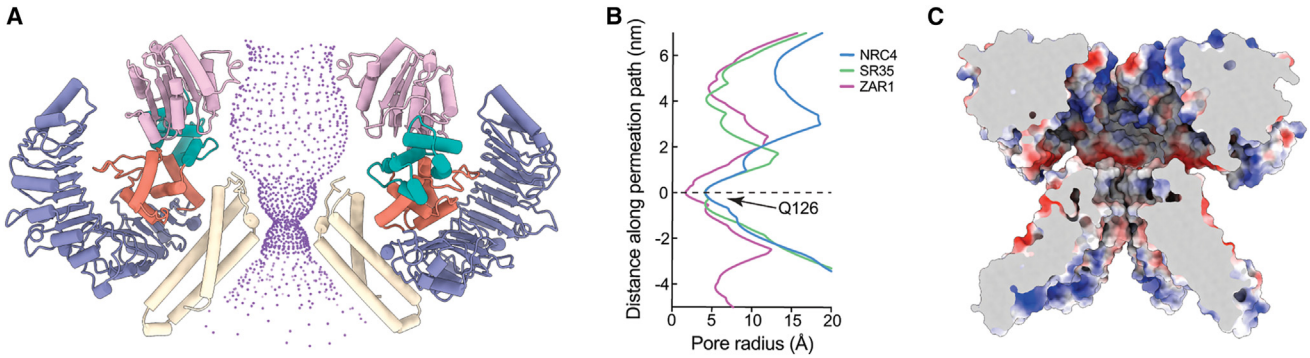

Figure 5. Structural analysis of ion permeation in the NRC4 resistosome

(A) The ion permeation path, calculated by HOLE,[39] for the active NRC4 resistosome is illustrated by purple dots. For clarity, only two protomers positioned diagonally opposite are displayed.

(B) A comparison of the corresponding pore radius of NRC4 (blue), Sr35 (green), and ZAR1 (magenta) resistosomes is presented, with the constriction site set as zero.

(C) A cross-sectional view of the ion-conducting pore within the NRC4 resistosome, shown as an electrostatic surface.

apparent in the active states of NRC4 or Sr35 structures, it is presumed to mediate Ca^{2+} influx, owing to analogous localization and hydrophobic properties[22] and its functional redundancy with the ZAR1 α1-helix noted above. Substituting the hydrophobic leucine with the longer, hydrophilic side chain of glutamines, as in ZAR1 noted above, alters the α1-helix from hydrophobic to hydrophilic. Notably, NRC4 still localizes on the PM.[47,48] Thus, this mutation is unlikely to prevent the α1-helix from integrating into the hydrophobic phospholipid bilayer of the membrane, but it demonstrably impairs the ability of NRC4 to function as an autonomous Ca^{2+} ion channel.

Dual-hexamer formation and potential immune regulation

Beyond the previously described hexameric resistosome, we identified a dodecameric state of NRC4 DV. This structure consists of two hexamers that come together to form a dumbbell-shaped dodecamer, resolved at 3.5 Å resolution (Figures S6A–S6C). Within this configuration, hydrophobic α1-helices from the CC domain, which typically integrate into the PM to initiate cell death, are instead internally associated, connecting the two hexamers (Figure S6D).[49,50] Co-immunoprecipitation assays confirmed this interaction, with FLAG-tagged and Twin-StrepTag II α1-helices showing mutual affinity (Figure S6E).

The double-layered structure of this dodecamer reflects the arrangement seen in the Sr35 resistosome from 2D analysis, implying that such higher-order arrangements may play a regulatory role in plant immune system.[14,15] Similarly, mouse NLRC4 can form a double-layer assembly, where its CARDs are buried at the center,[40] potentially restraining its role in immune response. Notably, mutations within the WHD domain of NLRC4, linked to auto-inflammatory disease in humans, are analogous to the DV mutation in the NRC4 WHD domain that induces cell death.[29,51–54] The comparable structural and functional dynamics of these double-layered assemblies lead to the hypothesis that the dodecameric state of the NRC4 resistosome may serve as a "protector" against undesired immune activation provoked by harmful mutations. Alternatively, this state may function as a "reservoir" for storing NRC4 protein without triggering an immune response. However, our blue native polyacrylamide gel electrophoresis (BN-PAGE) assays did not detect the dodecameric form in the native cellular environment (Figure S6F), suggesting its rarity or an artifact of cryo-EM sample preparation, a hypothesis to be investigated further.

NRCs switch between off and on states in plant immunity

Understanding the structural dynamics of NRC4 is essential for deciphering its function in plant immune responses. Previous cryo-EM studies revealed that NRC2 adopts a homodimeric formation in its pre-activation state.[55,56] Similarly, our BN-PAGE assays and negative staining results indicated that wild-type NRC4 also exists as an inactive homodimer (Figure S6F). These results align with the theory that NRCs undergo oligomerization as a mechanism of activation. The structural model for inactive NRC4 was predicted based on the NRC2 homodimer (Figure S6G).[55] In contrast to our observations in the NRC4 resistosome, homodimer formation occurs through the interaction between the NBD domain and the LRR domain. Furthermore, in the inactive state, the CC domains are absent, likely because they are flexible in the solvent and do not pack against each other as seen in the active state (Figures 2A and 2B). Additionally, a comparison of the NRC4 structure with the NRC2 structure (PDB: 8RFH) revealed very similar architectures[55] (with an RMSD of 1.052), implying that the NRC4 resistosome likely shares a similar mechanism of switching from inactive to active states with NRC2 (Figure S6H).

Upon activation, NCR4, NRC0, NRC2, and NRC3 transition into an active hexameric resistosome, as shown by our EM findings (Figures S1A and S6I–S6M). The 2D class averages consistently showed that all three NRC4 paralogs adopt an NRC4-like hexameric configuration (Figures S6I–S6K), suggesting a comparable overall architecture and possibly similar functionality across the NRC family.

Please cite this article in press as: Liu et al., Activation of the helper NRC4 immune receptor forms a hexameric resistosome, Cell (2024), https://doi.org/10.1016/j.cell.2024.07.013

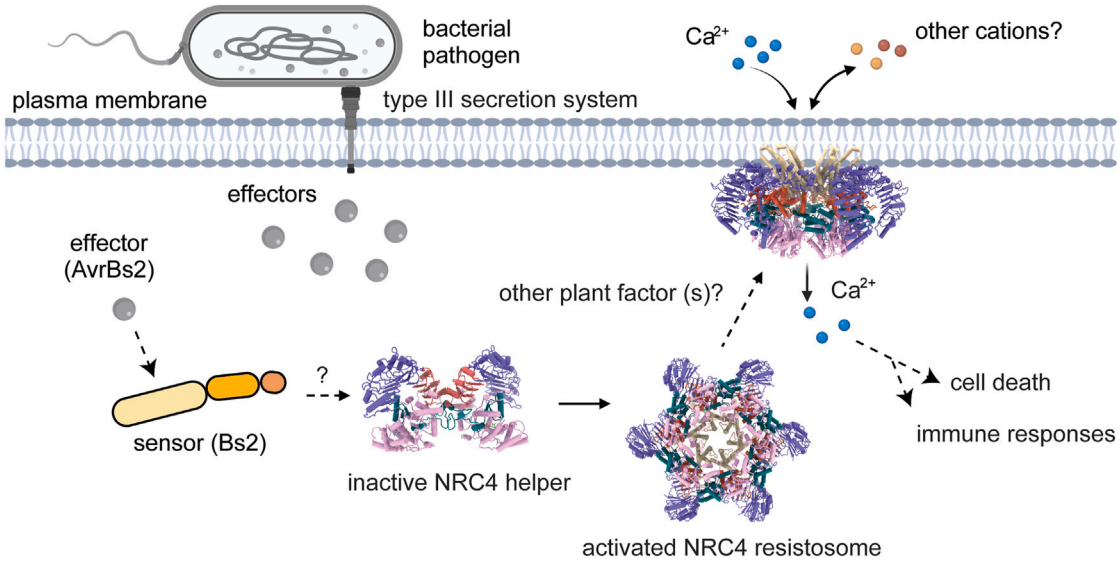

Figure 6. The NRC4 resistosome converges on Ca^{2+} influx in plant immunity

The figure illustrates the working model for NRC4 activation. NRC4 initially exists as a homodimer in its resting state. Upon activation by the upstream sNLR Bs2 and the pathogenic effector AvrBs2, NRC4 converts into a hexameric resistosome. The formation of this hexameric resistosome leads to Ca^{2+} influx in plant immune responses, probably involving other plant-specific factor(s). This mechanism is distinct from previously identified resistosomes such as ZAR1, Sr35, and NRG1, which form calcium channels allowing Ca^{2+} influx.

See also Figure S6.

Plant NLR signaling: Insights into Ca^{2+} influx as a central mechanism

Both CNL- and TNL-mediated immune responses in plant cells converge on Ca^{2+} influx, indicating that Ca^{2+} serves as a common messenger for plant NLR signaling.[14,22,28] Previous studies demonstrated that two sNLR resistosomes, ZAR1 and Sr35, as well as the hNLR NRG1 resistosome, can form Ca^{2+} permeable channels.[14,22,28] Two independent groups reported that the NRC4 DV resistosome exhibits a punctate distribution that is primarily associated with the PM, a pattern similar to that of the hNLR NRG1 resistosome.[28,47,48] Indeed, NRC4 DV, like NRG1.1 DV, triggered a robust Ca^{2+} influx when expressed in plants. Taken together, these findings suggested that NRC4 DV resistosomes might also form Ca^{2+}-permeable channels in plants, thereby triggering immune responses and cell death. However, neither NRC4 DV nor activation mimics NRC2 HR or NRC3 DV could form autonomous Ca^{2+} channels in two experimental systems. Thus, NRCs are likely to function differently in heterologous cells compared with NRG1.1 DV, indicating a possible requirement for plant-specific factors for their effective association with the PM. This may represent an activation mechanism of NRC hNLRs distinct from that of the NRG1.1-type hNLRs and warrants further research.

In summary, we describe the activation and function dynamics of the NRC4 resistosome, which transitions from a homodimer in its resting state to a hexameric structure upon activation by upstream sNLRs and pathogenic effectors. We also illustrate that the hexameric NRC4 resistosome is part of a complex that forms a channel permeable to Ca^{2+}, initiating an immune response (Figure 6). These results provide a mechanistic model of hNLR resistosome formation and regulation, offering the promise of advancing our understanding of plant pathogen defense mechanisms.

Limitations of the study

Our study revealed a hexameric arrangement of the NRC4 resistosome, distinct from previously reported resistosomes. However, significant gaps remain in our understanding. The mechanisms by which sNLRs deliver signals to the hNLRs and activate them, as well as the process by which hNLRs are activated and/or translocated to the PM, remain unknown. Although our research focuses on bacterial pathogens, NRCs can assist various sNLRs in detecting a broad range of pathogens. Further studies are needed to confirm this working model for NRCs in different pathogenic contexts. We also identified a potential inactive dodecamer state of NRC4; however, further investigation is needed to explore the *in vivo* presence of the NRC4 dodecamer structure and its biological significance. Unfortunately, mutagenesis efforts to investigate this aspect are challenging, as mutations disrupting dodecameric assembly would also affect hexamer assembly, membrane interaction, pore formation, and more. Additionally, while NRC resistosomes expressed in plant cells mediated Ca^{2+} influx crucial for the HR and cell death, NRC4 did not associate with the PM and or induce subsequent Ca^{2+} influx or cell death in animal cells. This suggests a requirement for additional plant-specific factor(s) for NRC-type NLRs compared with other reported plant resistosomes, warranting further investigation. Furthermore, we cannot rule out the possibility that other Ca^{2+} channels are activated. Given the recent identification of a small molecule (inositol

hexakisphosphate [IP6] or pentakisphosphate [IP5]) in the auto-inhibited NRC2 dimer[56] and an ATP in the activated NRC2 hexamer,[57] we analyzed our structural data of the activation mimic NRC4 structure. Although we identified density in the expected location, neither IP5,6 nor ATP fit perfectly, necessitating further study for confirmation.

STAR★METHODS

Detailed methods are provided in the online version of this paper and include the following:

- KEY RESOURCES TABLE
- RESOURCE AVAILABILITY
  - Lead contact
  - Materials availability
  - Data and code availability
- EXPERIMENTAL MODEL AND SUBJECT DETAILS
  - Plant materials and growth conditions
  - Bacterial strains and growth conditions
- METHOD DETAILS
  - Plasmid construction
  - Protein expression and detection in *N. benthamiana*
  - Protein expression and purification
  - BN-PAGE assay
  - Negative staining of NRC resistosome
  - Cryo-EM sample preparation and data collection
  - Cryo-EM data processing
  - Model building and validation
  - In planta Ca^{2+} influx assay
  - Cell viability assays
  - Fluorescence microscopy assay
  - Imaging of $[Ca^{2+}]_{cyt}$ in HEK293T cells
  - *Xenopus* oocyte electrophysiology
- QUANTIFICATION AND STATISTICAL ANALYSIS

SUPPLEMENTAL INFORMATION

Supplemental information can be found online at https://doi.org/10.1016/j.cell.2024.07.013.

ACKNOWLEDGMENTS

We thank R. Vance for his helpful comments and suggestions; D. Toso, R. Thakkar, and P. Tobias at the Cal-Cryo facility for their assistance with cryo-EM data collection and handling; staff at the Electron Microscope Laboratory for their assistance in EM sample preparation; K. Stine for computational support; and P. Cao for advice on cryo-EM grid preparation and data analysis. Transgenic *N. benthamiana* seeds carrying GCaMP3 were kindly provided by K. Yoshioka, and oocytes were kindly provided by E. Isacoff. Some illustrations were created with BioRender.com. Funding support for B.J.S. was provided by the Foundation for Food and Agriculture Research, the 2Blades Foundation, and the Innovative Genomics Institute Founders Fund. S.L. is supported by the National Institutes of Health R01GM138401. E.N. and J.L.D. are Howard Hughes Medical Institute investigators.

AUTHOR CONTRIBUTIONS

F.L., B.J.S., and Z. Yang conceived the project. F.L., Z.Y., C.W., Z. You, W.Q., J.H., and P.J. performed the experiments, analyzed the data, and prepared figures and tables. F.L., Z. Yang, C.W., and B.J.S. wrote the manuscript with contributions from all authors. All authors provided comments for the manuscript before submission.

DECLARATION OF INTERESTS

B.J.S. is a scientific co-founder of and serves on the board of directors for Mendel Biotechnology. He also serves on the scientific advisory boards of Verinomics and the Sainsbury Laboratory.

Received: March 4, 2024
Revised: June 6, 2024
Accepted: July 7, 2024
Published: August 1, 2024

REFERENCES

1. Ngou, B.P.M., Ding, P., and Jones, J.D.G. (2022). Thirty years of resistance: Zig-zag through the plant immune system. Plant Cell *34*, 1447–1478. https://doi.org/10.1093/plcell/koac041.
2. Jones, J.D.G., Vance, R.E., and Dangl, J.L. (2016). Intracellular innate immune surveillance devices in plants and animals. Science *354*, aaf6395. https://doi.org/10.1126/science.aaf6395.
3. Locci, F., and Parker, J.E. (2024). Plant NLR immunity activation and execution: a biochemical perspective. Open Biol. *14*, 230387. https://doi.org/10.1098/rsob.230387.
4. Jones, J.D.G., Staskawicz, B.J., and Dangl, J.L. (2024). The plant immune system: From discovery to deployment. Cell *187*, 2095–2116. https://doi.org/10.1016/j.cell.2024.03.045.
5. Yuan, M., Jiang, Z., Bi, G., Nomura, K., Liu, M., Wang, Y., Cai, B., Zhou, J.M., He, S.Y., and Xin, X.F. (2021). Pattern-recognition receptors are required for NLR-mediated plant immunity. Nature *592*, 105–109. https://doi.org/10.1038/s41586-021-03316-6.
6. Ngou, B.P.M., Ahn, H.K., Ding, P., and Jones, J.D.G. (2021). Mutual potentiation of plant immunity by cell-surface and intracellular receptors. Nature *592*, 110–115. https://doi.org/10.1038/s41586-021-03315-7.
7. Tian, H., Wu, Z., Chen, S., Ao, K., Huang, W., Yaghmaiean, H., Sun, T., Xu, F., Zhang, Y., Wang, S., et al. (2021). Activation of TIR signalling boosts pattern-triggered immunity. Nature *598*, 500–503. https://doi.org/10.1038/s41586-021-03987-1.
8. Pruitt, R.N., Locci, F., Wanke, F., Zhang, L., Saile, S.C., Joe, A., Karelina, D., Hua, C., Fröhlich, K., Wan, W.L., et al. (2021). The EDS1-PAD4-ADR1 node mediates Arabidopsis pattern-triggered immunity. Nature *598*, 495–499. https://doi.org/10.1038/s41586-021-03829-0.
9. Kourelis, J., Contreras, M.P., Harant, A., Pai, H., Lüdke, D., Adachi, H., Derevnina, L., Wu, C.H., and Kamoun, S. (2022). The helper NLR immune protein NRC3 mediates the hypersensitive cell death caused by the cell-surface receptor Cf-4. PLoS Genet. *18*, e1010414. https://doi.org/10.1371/journal.pgen.1010414.
10. Feehan, J.M., Wang, J., Sun, X., Choi, J., Ahn, H.K., Ngou, B.P.M., Parker, J.E., and Jones, J.D.G. (2023). Oligomerization of a plant helper NLR requires cell-surface and intracellular immune receptor activation. Proc. Natl. Acad. Sci. USA *120*, e2210406120. https://doi.org/10.1073/pnas.2210406120.
11. Wang, J., Hu, M., Wang, J., Qi, J., Han, Z., Wang, G., Qi, Y., Wang, H.W., Zhou, J.M., and Chai, J. (2019). Reconstitution and structure of a plant NLR resistosome conferring immunity. Science *364*, eaav5870. https://doi.org/10.1126/science.aav5870.
12. Martin, R., Qi, T., Zhang, H., Liu, F., King, M., Toth, C., Nogales, E., and Staskawicz, B.J. (2020). Structure of the activated ROQ1 resistosome directly recognizing the pathogen effector XopQ. Science *370*, eabd9993. https://doi.org/10.1126/science.abd9993.
13. Ma, S., Lapin, D., Liu, L., Sun, Y., Song, W., Zhang, X., Logemann, E., Yu, D., Wang, J., Jirschitzka, J., et al. (2020). Direct pathogen-induced assembly of an NLR immune receptor complex to form a holoenzyme. Science *370*, eabe3069. https://doi.org/10.1126/science.abe3069.
14. Förderer, A., Li, E., Lawson, A.W., Deng, Y.N., Sun, Y., Logemann, E., Zhang, X., Wen, J., Han, Z., Chang, J., et al. (2022). A wheat resistosome

defines common principles of immune receptor channels. Nature *610*, 532–539. https://doi.org/10.1038/s41586-022-05231-w.

15. Zhao, Y.B., Liu, M.X., Chen, T.T., Ma, X., Li, Z.K., Zheng, Z., Zheng, S.R., Chen, L., Li, Y.Z., Tang, L.R., et al. (2022). Pathogen effector AvrSr35 triggers Sr35 resistosome assembly via a direct recognition mechanism. Sci. Adv. *8*, eabq5108. https://doi.org/10.1126/sciadv.abq5108.
16. Huang, S., Jia, A., Song, W., Hessler, G., Meng, Y., Sun, Y., Xu, L., Laessle, H., Jirschitzka, J., Ma, S., et al. (2022). Identification and receptor mechanism of TIR-catalyzed small molecules in plant immunity. Science *377*, eabq3297. https://doi.org/10.1126/science.abq3297.
17. Jia, A., Huang, S., Song, W., Wang, J., Meng, Y., Sun, Y., Xu, L., Laessle, H., Jirschitzka, J., Hou, J., et al. (2022). TIR-catalyzed ADP-ribosylation reactions produce signaling molecules for plant immunity. Science *377*, eabq8180. https://doi.org/10.1126/science.abq8180.
18. Yu, D., Song, W., Tan, E.Y.J., Liu, L., Cao, Y., Jirschitzka, J., Li, E., Logemann, E., Xu, C., Huang, S., et al. (2022). TIR domains of plant immune receptors are 2′,3′-cAMP/cGMP synthetases mediating cell death. Cell *185*, 2370–2386.e18. https://doi.org/10.1016/j.cell.2022.04.032.
19. Horsefield, S., Burdett, H., Zhang, X., Manik, M.K., Shi, Y., Chen, J., Qi, T., Gilley, J., Lai, J.S., Rank, M.X., et al. (2019). NAD(+) cleavage activity by animal and plant TIR domains in cell death pathways. Science *365*, 793–799. https://doi.org/10.1126/science.aax1911.
20. Wan, L., Essuman, K., Anderson, R.G., Sasaki, Y., Monteiro, F., Chung, E.H., Osborne Nishimura, E., DiAntonio, A., Milbrandt, J., Dangl, J.L., and Nishimura, M.T. (2019). TIR domains of plant immune receptors are NAD(+)-cleaving enzymes that promote cell death. Science *365*, 799–803. https://doi.org/10.1126/science.aax1771.
21. Manik, M.K., Shi, Y., Li, S., Zaydman, M.A., Damaraju, N., Eastman, S., Smith, T.G., Gu, W., Masic, V., Mosaiab, T., et al. (2022). Cyclic ADP ribose isomers: Production, chemical structures, and immune signaling. Science *377*, eadc8969. https://doi.org/10.1126/science.adc8969.
22. Bi, G., Su, M., Li, N., Liang, Y., Dang, S., Xu, J., Hu, M., Wang, J., Zou, M., Deng, Y., et al. (2021). The ZAR1 resistosome is a calcium-permeable channel triggering plant immune signaling. Cell *184*, 3528–3541.e12. https://doi.org/10.1016/j.cell.2021.05.003.
23. Peart, J.R., Mestre, P., Lu, R., Malcuit, I., and Baulcombe, D.C. (2005). NRG1, a CC-NB-LRR protein, together with N, a TIR-NB-LRR protein, mediates resistance against tobacco mosaic virus. Curr. Biol. *15*, 968–973. https://doi.org/10.1016/j.cub.2005.04.053.
24. Bonardi, V., Tang, S., Stallmann, A., Roberts, M., Cherkis, K., and Dangl, J.L. (2011). Expanded functions for a family of plant intracellular immune receptors beyond specific recognition of pathogen effectors. Proc. Natl. Acad. Sci. USA *108*, 16463–16468. https://doi.org/10.1073/pnas.1113726108.
25. Wu, C.H., Abd-El-Haliem, A., Bozkurt, T.O., Belhaj, K., Terauchi, R., Vossen, J.H., and Kamoun, S. (2017). NLR network mediates immunity to diverse plant pathogens. Proc. Natl. Acad. Sci. USA *114*, 8113–8118. https://doi.org/10.1073/pnas.1702041114.
26. Contreras, M.P., Pai, H., Tumtas, Y., Duggan, C., Yuen, E.L.H., Cruces, A.V., Kourelis, J., Ahn, H.K., Lee, K.T., Wu, C.H., et al. (2023). Sensor NLR immune proteins activate oligomerization of their NRC helpers in response to plant pathogens. EMBO J. *42*, e111519. https://doi.org/10.15252/embj.2022111519.
27. Ahn, H.K., Lin, X., Olave-Achury, A.C., Derevnina, L., Contreras, M.P., Kourelis, J., Wu, C.H., Kamoun, S., and Jones, J.D.G. (2023). Effector-dependent activation and oligomerization of plant NRC class helper NLRs by sensor NLR immune receptors Rpi-amr3 and Rpi-amr1. EMBO J. *42*, e111484. https://doi.org/10.15252/embj.2022111484.
28. Jacob, P., Kim, N.H., Wu, F., El-Kasmi, F., Chi, Y., Walton, W.G., Furzer, O.J., Lietzan, A.D., Sunil, S., Kempthorn, K., et al. (2021). Plant "helper" immune receptors are Ca(2+)-permeable nonselective cation channels. Science *373*, 420–425. https://doi.org/10.1126/science.abg7917.
29. Adachi, H., Contreras, M.P., Harant, A., Wu, C.H., Derevnina, L., Sakai, T., Duggan, C., Moratto, E., Bozkurt, T.O., Maqbool, A., et al. (2019). An N-terminal motif in NLR immune receptors is functionally conserved across distantly related plant species. eLife *8*, e49956. https://doi.org/10.7554/eLife.49956.
30. Williams, S.J., Sornaraj, P., deCourcy-Ireland, E., Menz, R.I., Kobe, B., Ellis, J.G., Dodds, P.N., and Anderson, P.A. (2011). An autoactive mutant of the M flax rust resistance protein has a preference for binding ATP, whereas wild-type M protein binds ADP. Mol. Plant Microbe Interact. *24*, 897–906. https://doi.org/10.1094/mpmi-03-11-0052.
31. Bentham, A., Burdett, H., Anderson, P.A., Williams, S.J., and Kobe, B. (2017). Animal NLRs provide structural insights into plant NLR function. Ann. Bot. *119*, 827-702. https://doi.org/10.1093/aob/mcw171.
32. Tameling, W.I.L., Vossen, J.H., Albrecht, M., Lengauer, T., Berden, J.A., Haring, M.A., Cornelissen, B.J.C., and Takken, F.L.W. (2006). Mutations in the NB-ARC domain of I-2 that impair ATP hydrolysis cause autoactivation. Plant Physiol. *140*, 1233–1245. https://doi.org/10.1104/pp.105.073510.
33. Rairdan, G.J., Collier, S.M., Sacco, M.A., Baldwin, T.T., Boettrich, T., and Moffett, P. (2008). The coiled-coil and nucleotide binding domains of the Potato Rx disease resistance protein function in pathogen recognition and signaling. Plant Cell *20*, 739–751. https://doi.org/10.1105/tpc.107.056036.
34. Wang, C., and Luan, S. (2024). Calcium homeostasis and signaling in plant immunity. Curr. Opin. Plant Biol. *77*, 102485. https://doi.org/10.1016/j.pbi.2023.102485.
35. Grant, M., Brown, I., Adams, S., Knight, M., Ainslie, A., and Mansfield, J. (2000). The RPM1 plant disease resistance gene facilitates a rapid and sustained increase in cytosolic calcium that is necessary for the oxidative burst and hypersensitive cell death. Plant J. *23*, 441–450. https://doi.org/10.1046/j.1365-313x.2000.00804.x.
36. Gao, X., Chen, X., Lin, W., Chen, S., Lu, D., Niu, Y., Li, L., Cheng, C., McCormack, M., Sheen, J., et al. (2013). Bifurcation of Arabidopsis NLR immune signaling via Ca^{2+}-dependent protein kinases. PLoS Pathog. *9*, e1003127. https://doi.org/10.1371/journal.ppat.1003127.
37. Wang, C., Tang, R.J., Kou, S., Xu, X., Lu, Y., Rauscher, K., Voelker, A., and Luan, S. (2024). Mechanisms of calcium homeostasis orchestrate plant growth and immunity. Nature *627*, 382–388. https://doi.org/10.1038/s41586-024-07100-0.
38. DeFalco, T.A., Toyota, M., Phan, V., Karia, P., Moeder, W., Gilroy, S., and Yoshioka, K. (2017). Using GCaMP3 to Study Ca2+ Signaling in Nicotiana Species. Plant Cell Physiol. *58*, 1173–1184. https://doi.org/10.1093/pcp/pcx053.
39. Smart, O.S., Neduvelil, J.G., Wang, X., Wallace, B.A., and Sansom, M.S. (1996). HOLE: a program for the analysis of the pore dimensions of ion channel structural models. J. Mol. Graph. *14*, 354–360. https://doi.org/10.1016/s0263-7855(97)00009-x.
40. Tenthorey, J.L., Haloupek, N., López-Blanco, J.R., Grob, P., Adamson, E., Hartenian, E., Lind, N.A., Bourgeois, N.M., Chacón, P., Nogales, E., and Vance, R.E. (2017). The structural basis of flagellin detection by NAIP5: A strategy to limit pathogen immune evasion. Science *358*, 888–893. https://doi.org/10.1126/science.aao1140.
41. Halff, E.F., Diebolder, C.A., Versteeg, M., Schouten, A., Brondijk, T.H.C., and Huizinga, E.G. (2012). Formation and structure of a NAIP5-NLRC4 inflammasome induced by direct interactions with conserved N- and C-terminal regions of flagellin. J. Biol. Chem. *287*, 38460–38472. https://doi.org/10.1074/jbc.M112.393512.
42. Zhang, L., Chen, S., Ruan, J., Wu, J., Tong, A.B., Yin, Q., Li, Y., David, L., Lu, A., Wang, W.L., et al. (2015). Cryo-EM structure of the activated NAIP2-NLRC4 inflammasome reveals nucleated polymerization. Science *350*, 404–409. https://doi.org/10.1126/science.aac5789.
43. Hu, Z., Zhou, Q., Zhang, C., Fan, S., Cheng, W., Zhao, Y., Shao, F., Wang, H.W., Sui, S.F., and Chai, J. (2015). Structural and biochemical basis for

induced self-propagation of NLRC4. Science *350*, 399–404. https://doi.org/10.1126/science.aac5489.

44. Huang, C.-Y., Huang, Y.-S., Sugihara, Y., Wang, H.-Y., Huang, L.-T., Lopez-Agudelo, J.C., Chen, Y.-F., Lin, K.-Y., Chiang, B.-J., Toghani, A., et al. (2023). Functional divergence shaped the network architecture of plant immune receptors. Preprint at bioRxiv. https://doi.org/10.1101/2023.12.12.571219.

45. Sundaram, B., Tweedell, R.E., Prasanth Kumar, S., and Kanneganti, T.D. (2024). The NLR family of innate immune and cell death sensors. Immunity *57*, 674–699. https://doi.org/10.1016/j.immuni.2024.03.012.

46. Contreras, M.P., Lüdke, D., Pai, H., Toghani, A., and Kamoun, S. (2023). NLR receptors in plant immunity: making sense of the alphabet soup. EMBO Rep. *24*, e57495. https://doi.org/10.15252/embr.202357495.

47. Duggan, C., Moratto, E., Savage, Z., Hamilton, E., Adachi, H., Wu, C.H., Leary, A.Y., Tumtas, Y., Rothery, S.M., Maqbool, A., et al. (2021). Dynamic localization of a helper NLR at the plant-pathogen interface underpins pathogen recognition. Proc. Natl. Acad. Sci. USA *118*. https://doi.org/10.1073/pnas.2104997118.

48. Wang, Z., Liu, X., Yu, J., Yin, S., Cai, W., Kim, N.H., El Kasmi, F., Dangl, J.L., and Wan, L. (2023). Plasma membrane association and resistosome formation of plant helper immune receptors. Proc. Natl. Acad. Sci. USA *120*, e2222036120. https://doi.org/10.1073/pnas.2222036120.

49. Jumper, J., Evans, R., Pritzel, A., Green, T., Figurnov, M., Ronneberger, O., Tunyasuvunakool, K., Bates, R., Žídek, A., Potapenko, A., et al. (2021). Highly accurate protein structure prediction with AlphaFold. Nature *596*, 583–589. https://doi.org/10.1038/s41586-021-03819-2.

50. Varadi, M., Anyango, S., Deshpande, M., Nair, S., Natassia, C., Yordanova, G., Yuan, D., Stroe, O., Wood, G., Laydon, A., et al. (2022). AlphaFold Protein Structure Database: massively expanding the structural coverage of protein-sequence space with high-accuracy models. Nucleic Acids Res. *50*, D439–D444. https://doi.org/10.1093/nar/gkab1061.

51. Canna, S.W., de Jesus, A.A., Gouni, S., Brooks, S.R., Marrero, B., Liu, Y., DiMattia, M.A., Zaal, K.J.M., Sanchez, G.A.M., Kim, H., et al. (2014). An activating NLRC4 inflammasome mutation causes autoinflammation with recurrent macrophage activation syndrome. Nat. Genet. *46*, 1140–1146. https://doi.org/10.1038/ng.3089.

52. Kitamura, A., Sasaki, Y., Abe, T., Kano, H., and Yasutomo, K. (2014). An inherited mutation in NLRC4 causes autoinflammation in human and mice. J. Exp. Med. *211*, 2385–2396. https://doi.org/10.1084/jem.20141091.

53. Romberg, N., Al Moussawi, K., Nelson-Williams, C., Stiegler, A.L., Loring, E., Choi, M., Overton, J., Meffre, E., Khokha, M.K., Huttner, A.J., et al. (2014). Mutation of NLRC4 causes a syndrome of enterocolitis and autoinflammation. Nat. Genet. *46*, 1135–1139. https://doi.org/10.1038/ng.3066.

54. Vance, R.E. (2015). The NAIP/NLRC4 inflammasomes. Curr. Opin. Immunol. *32*, 84–89. https://doi.org/10.1016/j.coi.2015.01.010.

55. Selvaraj, M., Toghani, A., Pai, H., Sugihara, Y., Kourelis, J., Yuen, E.L.H., Ibrahim, T., Zhao, H., Xie, R., Maqbool, A., et al. (2023). Activation of plant immunity through conversion of a helper NLR homodimer into a resistosome. Preprint at bioRxiv. https://doi.org/10.1101/2023.12.17.572070.

56. Ma, S., An, C., Lawson, A.W., Cao, Y., Sun, Y., Tan, E.Y.J., Pan, J., Jirschitzka, J., Kümmel, F., Mukhi, N., et al. (2024). Oligomerization-mediated autoinhibition and cofactor binding of a plant NLR. Nature, 20240612. https://doi.org/10.1038/s41586-024-07668-7.

57. Madhuprakash, J., Toghani, A., Contreras, M.P., Posbeyikian, A., Richardson, J., Kourelis, J., Bozkurt, T.O., Webster, M., and Kamoun, S. (2024). A disease resistance protein triggers oligomerization of its NLR helper into a hexameric resistosome to mediate innate immunity. Preprint at bioRxiv. https://doi.org/10.1101/2024.06.18.599586.

58. Zhang, Y., Chen, M., Siemiatkowska, B., Toleco, M.R., Jing, Y., Strotmann, V., Zhang, J., Stahl, Y., and Fernie, A.R. (2020). A Highly Efficient Agrobacterium-Mediated Method for Transient Gene Expression and Functional Studies in Multiple Plant Species. Plant Commun. *1*, 100028. https://doi.org/10.1016/j.xplc.2020.100028.

59. Martin, R., Liu, F., and Staskawicz, B. (2022). Isolation of Protein Complexes from Tobacco Leaves by a Two-Step Tandem Affinity Purification. Curr. Protoc. *2*, e572. https://doi.org/10.1002/cpz1.572.

60. Na Ayutthaya, P.P., Lundberg, D., Weigel, D., and Li, L. (2020). Blue Native Polyacrylamide Gel Electrophoresis (BN-PAGE) for the Analysis of Protein Oligomers in Plants. Curr. Protoc. Plant Biol. *5*, e20107. https://doi.org/10.1002/cppb.20107.

61. Carragher, B., Kisseberth, N., Kriegman, D., Milligan, R.A., Potter, C.S., Pulokas, J., and Reilein, A. (2000). Leginon: an automated system for acquisition of images from vitreous ice specimens. J. Struct. Biol. *132*, 33–45. https://doi.org/10.1006/jsbi.2000.4314.

62. Kimanius, D., Dong, L., Sharov, G., Nakane, T., and Scheres, S.H.W. (2021). New tools for automated cryo-EM single-particle analysis in RELION-4.0. Biochem. J. *478*, 4169–4185. https://doi.org/10.1042/bcj20210708.

63. Punjani, A., Rubinstein, J.L., Fleet, D.J., and Brubaker, M.A. (2017). cryoSPARC: algorithms for rapid unsupervised cryo-EM structure determination. Nat. Methods *14*, 290–296. https://doi.org/10.1038/nmeth.4169.

64. Pettersen, E.F., Goddard, T.D., Huang, C.C., Meng, E.C., Couch, G.S., Croll, T.I., Morris, J.H., and Ferrin, T.E. (2021). UCSF ChimeraX: Structure visualization for researchers, educators, and developers. Protein Sci. *30*, 70–82. https://doi.org/10.1002/pro.3943.

65. Goddard, T.D., Huang, C.C., Meng, E.C., Pettersen, E.F., Couch, G.S., Morris, J.H., and Ferrin, T.E. (2018). UCSF ChimeraX: Meeting modern challenges in visualization and analysis. Protein Sci. *27*, 14–25. https://doi.org/10.1002/pro.3235.

66. Meng, E.C., Goddard, T.D., Pettersen, E.F., Couch, G.S., Pearson, Z.J., Morris, J.H., and Ferrin, T.E. (2023). UCSF ChimeraX: Tools for structure building and analysis. Protein Sci. *32*, e4792. https://doi.org/10.1002/pro.4792.

67. Emsley, P., and Cowtan, K. (2004). Coot: model-building tools for molecular graphics. Acta Crystallogr. D Biol. Crystallogr. *60*, 2126–2132. https://doi.org/10.1107/s0907444904019158.

68. Adams, P.D., Afonine, P.V., Bunkóczi, G., Chen, V.B., Davis, I.W., Echols, N., Headd, J.J., Hung, L.W., Kapral, G.J., Grosse-Kunstleve, R.W., et al. (2010). PHENIX: a comprehensive Python-based system for macromolecular structure solution. Acta Crystallogr. D Biol. Crystallogr. *66*, 213–221. https://doi.org/10.1107/s0907444909052925.

Please cite this article in press as: Liu et al., Activation of the helper NRC4 immune receptor forms a hexameric resistosome, Cell (2024), https://doi.org/10.1016/j.cell.2024.07.013

STAR★METHODS

KEY RESOURCES TABLE

REAGENT or RESOURCE	SOURCE	IDENTIFIER
Antibodies		
Anti-FLAG M2 Affinity Gel	Millipore Sigma	Cat# A2220; RRID: AB_10063035
Mouse anti-Flag-HRP	Millipore Sigma	Cat# A8592; RRID: AB_439702
Rat anti-mCherry	ThermoFisher scientific	Cat# M11217; RRID: AB_2536611
Mouse anti-Strep Tag II-HRP	Millipore Sigma	Cat# 71591-3; RRID: AB_10806716
HA Tag Polyclonal antibody	Invitrogen	Cat# 14-6756-81; RRID:AB_468301
Goat Anti-Rabbit IgG-HRP	GeneTex	Cat# GTX213110-01; RRID:AB_10618573
Strep-Tactin XT 4Flow high capacity resin	iBa	Cat# 2-5030-002
Bacterial and Virus Strains		
Agrobacterium tumefaciens AGL1	Laboratory stock	N/A
Escherichia coli DH5a	NEB	Cat# C2987H
Chemicals, Peptides, and Recombinant Proteins		
Pierce 3x DYKDDDK Peptide	ThermoFisher scientific	Cat# A36806
DMSO	ThermoFisher scientific	Cat# BP231-100
Bestatin	Goldbio	Cat# B-915-100
HEPES	Millipore Sigma	Cat# 7365-45-9
EDTA	Millipore Sigma	Cat# 6381-92-6
$MgCl_2$	Millipore Sigma	Cat# 7791-18-6
NaCl	Millipore Sigma	Cat# 7647-14-5
KCl	Millipore Sigma	Cat# 7447-40-7
NP-40	ThermoFisher scientific	Cat# 85124
glycerol	ThermoFisher scientific	Cat# 56-81-5
E-64	Goldbio	Cat# E-064-5
MES	Millipore Sigma	Cat# 145224-94-8
gentamicin	Goldbio	Cat# G-400
kanamycin	Goldbio	Cat# K-120
leupeptin	Goldbio	Cat# L-010-5
aprotinin	Millipore Sigma	Cat# A-6279
Pepstatin A	Goldbio	Cat# P-020-5
1,10-phenanthroline	Goldbio	Cat# P980-10
phosphoramidon	Millipore Sigma	Cat# R7385
PMSF	Goldbio	Cat# P-470-10
Rifampicin	Goldbio	Cat# R-120-1
Biotin	Millipore Sigma	Cat# B4501
DTT	Goldbio	Cat# 27565-41-9
Cesium chloride	Millipore Sigma	Cat# 289329-25G
Tetraethylammonium chloride	Millipore Sigma	Cat# T2265-25G
Lanthanum(III) Chloride	Millipore Sigma	Cat# 262072-25G
Ruthenium Red	Millipore Sigma	Cat# R2751-1G
Piece™ IP-lysis buffer	ThermoFisher scientific	Cat# 87787
1X protease inhibitor cocktail	ThermoFisher scientific	Cat# 1861279
4X Laemmli Sample buffer	Bio-Rad	Cat# 1610747
ProSignal® Femto ECL reagent	Genesee Scientific	Cat# 20-300B
InstantBlue	abcam	Cat# ab119211

(*Continued on next page*)

Please cite this article in press as: Liu et al., Activation of the helper NRC4 immune receptor forms a hexameric resistosome, Cell (2024), https://doi.org/10.1016/j.cell.2024.07.013

Continued

REAGENT or RESOURCE	SOURCE	IDENTIFIER
Deposited Data		
hexameric NRC4 resistosome	This paper	PDB: 9CC8; EMDB: EMD-45437
dodecameric NRC4 resistosome	This paper	PDB: 9CC9; EMDB: EMD-45438
Experimental Models: Cell Lines		
Human: HEK293 FT	Thermo Fisher scientific	Cat# R70007
Human: HEK293 T	Tissue Culture facility at UNC, Lineberger Comprehensive Cancer Center	N/A
Experimental Models: Organisms/Strains		
Xenopus oocyte	Laboratory stock of E.I.	N/A
Nicotiana benthamiana	Laboratory stock	N/A
Oligonucleotides		
Primers used in this study, see Table S1	This paper	N/A
Recombinant DNA		
pAS39:35s::NRC4 L9E DV eGFP-3XFlag	This paper	N/A
pAS39:35s::NRC4 L9E DV eGFP-Twin StrepTag II	This paper	N/A
pAS39:35s::NRC4 DV eGFP-3XFlag	This paper	N/A
pAS39:35s::NRC4 L9E eGFP-3XFlag	This paper	N/A
pAS39:35s::NRC4 eGFP-3XFlag	This paper	N/A
pAS39:35s::NRC4-StrepTag II	This paper	N/A
pAS39:35s::NRC4 L9E-StrepTag II	This paper	N/A
pAS39:35s::NRC4 L9E DV-StrepTag II	This paper	N/A
pAS39:35s::NRC4 DV-StrepTag II	This paper	N/A
pAS39:35s::NRC4 DV-H40A/D47A/Q129A-StrepTag II	This paper	N/A
pAS39:35s::NRC4 H40A/D47A/Q129A-StrepTag II	This paper	N/A
pAS39:35s::NRC4 DV-H40A-StrepTag II	This paper	N/A
pAS39:35s::NRC4 DV-D47A-StrepTag II	This paper	N/A
pAS39:35s::NRC4 DV-Q129A-StrepTag II	This paper	N/A
pAS39:35s::NRC4 DV-D275A/E283A/D453A-StrepTag II	This paper	N/A
pAS39:35s::NRC4-D275A/E283A/D453A-StrepTag II	This paper	N/A
pAS39:35s::NRC4 DV-D275A-StrepTag II	This paper	N/A
pAS39:35s::NRC4 DV-E283A-StrepTag II	This paper	N/A
pAS39:35s::NRC4 DV-D453A-StrepTag II	This paper	N/A
pAS39:35s::NRC4 DV-C661A-StrepTag II	This paper	N/A
pAS39:35s::NRC4 DV-K190A/T191A/T192A/R295A-StrepTag II	This paper	N/A
pAS39:35s::NRC4-K190A/T191A/T192A/R295A-StrepTag II	This paper	N/A
pAS39:35s::NRC4 DV-K190A-StrepTag II	This paper	N/A
pAS39:35s::NRC4 DV-T191A-StrepTag II	This paper	N/A
pAS39:35s::NRC4-T191A-StrepTag II	This paper	N/A
pAS39:35s::NRC4 DV-T192A-StrepTag II	This paper	N/A
pAS39:35s::NRC4 DV-R295A-StrepTag II	This paper	N/A
pAS39:35s::NRC4 DV-E731A/D74A/D77A-StrepTag II	This paper	N/A
pAS39:35s::NRC4-E731A/D74A/D77A-StrepTag II	This paper	N/A
pAS39:35s::NRC4 DV-E731A-StrepTag II	This paper	N/A
pAS39:35s::NRC4 DV-D74A-StrepTag II	This paper	N/A
pAS39:35s::NRC4 DV-D77A-StrepTag II	This paper	N/A
pAS39:35s::NRC4 DV-R514A/R537A-StrepTag II	This paper	N/A
pAS39:35s::NRC4-R514A/R537A-StrepTag II	This paper	N/A
pAS39:35s::NRC4 DV-R514A-StrepTag II	This paper	N/A

(*Continued on next page*)

Please cite this article in press as: Liu et al., Activation of the helper NRC4 immune receptor forms a hexameric resistosome, Cell (2024), https://doi.org/10.1016/j.cell.2024.07.013

Continued

REAGENT or RESOURCE	SOURCE	IDENTIFIER
pAS39:35s::NRC4-R514A-StrepTag II	This paper	N/A
pAS39:35s::NRC4 DV-R537A-StrepTag II	This paper	N/A
pAS39:35s::NRC4-R537A-StrepTag II	This paper	N/A
pAS39:35s::NRC4-L9E eGFP-HA	This paper	N/A
pAS39:35s::Bs2-HA	This paper	N/A
pAS39:35s::AvrBs2-HA	This paper	N/A
pAS39:35s::NRC2-L17E -3XFlag	This paper	N/A
pAS39:35s::NRC3-L21E-3xFlag	This paper	N/A
pAS39:35s::NRC0-EEE-3XFlag	This paper	N/A
pAS39:35s::NRC0S-StrepTag II	This paper	N/A
prk5m-NRC2 HR-mCherry-myc	This paper	N/A
prk5m-NRC3 DV-mCherry-myc	This paper	N/A
prk5m-NRC4 DV-mCherry-myc	This paper	N/A
prk5m-NRG1.1 DV-mCherry-myc	This paper	N/A
pGEMHE-AvrBs2-BFP-StrepTag II	This paper	N/A
pGEMHE-Bs2-mNeon-Flag	This paper	N/A
pGEMHE-NRC4-mCherry-myc	This paper	N/A
pGEMHE-NRC4 DV-mCherry-myc	This paper	N/A
pGEMHE-NRG1.1 DV-mCherry-myc	This paper	N/A
pAS39:35s::NRC4 D47A-StrepTag II	This paper	N/A
Software and Algorithms		
COOT	Emsley et al.[67]	https://www2.mrc-lmb.cam.ac.uk/personal/pemsley/coot/
GraphPad Prism 8.0	GraphPad Software	https://www.graphpad.com/
PyMOL	PyMOL software	https://www.pymol.org/
CryoSPARC	Punjani et al.[63]	https://cryosparc.com/
ChimeraX	Pettersen et al.[64]	https://www.cgl.ucsf.edu/chimera/
AlphaFold Multimer	Jumper et al.[49]	https://alphafold.ebi.ac.uk/
PHENIX	Adams et al.[68]	https://www.phenix-online.org/
RELION	Kimanius et al.[62]	https://www2.mrclmb.cam.ac.uk/relion/

RESOURCE AVAILABILITY

Lead contact

Further information and requests for resources and reagents should be directed to and will be fulfilled by the lead contact, Brian J. Staskawicz (stask@berkeley.edu).

Materials availability

All the plasmids generated in this study are available from Brian J. Staskawicz upon request under a materials transfer agreement with University of California, Berkeley

Data and code availability

The cryo-EM maps of the hexameric and dodecameric NRC4 resistosome are deposited in the EMDB database with accession numbers of EMD-45437 and EMD-45438, respectively. The atomic models of the dimer, hexameric and dodecameric NRC4 resistosome are deposited in the PDB database with accession number of 9CC8 and 9CC9, respectively. This paper does not report original code.

EXPERIMENTAL MODEL AND SUBJECT DETAILS

Plant materials and growth conditions

Wild-type *N. benthamiana* plants were cultivated in a controlled growth chamber within an 8-hou light/16-hour dark photoperiod at 23°C. For the HR assay, 4-week-old *N. benthamiana* plants were used. The *Agrobacterium* strains containing the plasmids were

Please cite this article in press as: Liu et al., Activation of the helper NRC4 immune receptor forms a hexameric resistosome, Cell (2024), https://doi.org/10.1016/j.cell.2024.07.013

infiltrated into leaves from the abaxial side, and HR phenotypes were observed and photographed approximately 1-2 days after infiltration.

Bacterial strains and growth conditions

The binary constructs were transformed into *Agrobacterium tumefaciens* strain AGL1, followed by cultivation in YEB (Yeast Extract Broth) at 28°C.[58] Antibiotics were added to the growth medium at the following concentrations (in mg/L): Kanamycin 50, Rifampicin 100, and Carbenicillin 100.

METHOD DETAILS

Plasmid construction

Using the Gibson based cloning system, the genes were cloned into the destination vectors for protein expression (key resources table). Primers used to amplify these sequences are listed in Table S1.

Protein expression and detection in *N. benthamiana*

Proteins were expressed in leaves of 4-5-week-old *N. benthamiana* plants through transient agroinfiltration. The *Agrobacterium* cultures were prepared as described.[58] For western blot analysis, two 10-mm leaf discs were collected for each sample 2 days after infiltration. The samples were immediately frozen in liquid nitrogen and ground into a fine powder. The ground samples were then resuspended in 200 μl of Piece™ IP-lysis buffer (Thermo Fisher Scientific) with 1X protease inhibitor cocktail (Thermo Fisher Scientific). With gentle rotation for 15 minutes at 4°C, total proteins were denatured by supplementing with the proper volume of 4X Laemmli Sample buffer (Bio-Rad). After centrifugation at 16,000 x *g* for 15 min, the supernatants were resolved using SDS-polyacrylamide gel electrophoresis (PAGE) followed by immunoblotting analysis using HRP-conjugated anti-StrepTag™II antibody (Sigma). In the co-immunoprecipitation assay, Strep-Tactin® XT 4Flow® high-capacity resin was used for the protein enrichment. The resins with immunoprecipitated proteins were then suspended in the proper volume of 4X laemmli sample buffer with heating at 95°C for 10 mins to elute proteins. Eluted proteins were subsequently resolved using SDS-PAGE, followed by immunoblotting analysis using HRP-conjugated ANTI-Flag M2 monoclonal antibody (Sigma). HA Tag Polyclonal antibody (Invitrogen) and goat anti-mouse IgG antibody (HRP) were used to detect the Bs2 and AvrBs2. The HRP signal was photographed using ProSignal® Femto ECL reagent (Genesee Scientific). InstantBlue® (abcam) Coomassie-stained membranes were photographed as loading controls for a similar amount of total proteins.

Protein expression and purification

Protein purification was conducted following a modified protocol based on a previously published method.[59] Vectors containing the NRC4 L9EDV, genetically fused to either a C-terminal 3XFlag or Twin-StrepTag II, were transformed into *Agrobacterium* AGL1. They were transiently co-expressed in the presence of the P19 suppressor in 4-5-week-old *N. benthamiana* leaves by agroinfiltration. Leaf tissue was harvested 2 days after infiltration, ground using a mortar and pestle, and then resuspended in a buffer containing protease inhibitors as described.[59] The lysate was further processed by sonication. The soluble fraction of the lysate was separated from cell debris by centrifugation at 20,000 x *g* for 45 minutes at 4°C. The supernatant was loaded onto a column with Macro-Prep DEAE Resin (Bio-Rad Laboratories) using a peristaltic pump (Gilson Incorporated). Sequential affinity chromatography was performed, first with Flag-immunoprecipitation (ANTI-Flag M2 Affinity Gel, Millipore Sigma), and then Strep-Tactin immunoprecipitation (Strep-Tactin® XT 4Flow® high capacity resin, IBA), to capture the protein complex. The purified proteins were subsequently analyzed using SDS-PAGE, as shown in Figure S1D.

BN-PAGE assay

The experiments were carried out according to protocol.[60] The samples were applied to Native PAGE 3%-12% Bis-Tris gels and run in parallel with the Native Mark™ unstained protein standard for reference (Invitrogen). After electrophoresis, the proteins were transferred to polyvinylidene difluoride (PVDF) membranes using NuPAGE™ transfer buffer. These proteins were then fixed onto the membranes by incubation in 8% acetic acid for 10 minutes, followed by washing, blocking and immunoblotting procedures. Flag-tagged or StrepTag II-tagged proteins were detected as previously described.

Negative staining of NRC resistosome

A total of 4 μL of purified protein was applied to freshly glow-discharged (Tergo™ EM PIE scientific) copper grids and incubated for 1 minute. Subsequently, the grid was washed in three 50 μL drops of 2% (w/v) uranyl formate for 5 seconds, followed by blotting and drying in the hood. The negative staining grids were screened using the Tecnai F20 microscope (Thermo Fisher Scientific). The best grids were selected for data collection utilizing Leginon software.[61] The negative staining data were processed in RELION software following the standard pipeline.[62] Particles representing the desired size were manually picked and subjected to two rounds of 2D classification. The class averages showed a clear hexameric configuration of NCR0, NRC2, NRC3, and NRC4 resistosome.

Please cite this article in press as: Liu et al., Activation of the helper NRC4 immune receptor forms a hexameric resistosome, Cell (2024), https://doi.org/10.1016/j.cell.2024.07.013

Cryo-EM sample preparation and data collection

For Cryo-EM sample preparation, Quantifoil Au 2/1 grids with a 2nm carbon layer, or Quantifoil Au 1.2/1.3 grids coated with a graphene layer, were utilized. The grids were glow discharged twice (25 + 10 seconds) at 15 mA. Subsequently, 3μl of freshly prepared NRC4 L9EDV protein was applied to the grids, followed by blotting for 5 seconds at 4 °C under 100% humidity conditions. The grids were then rapidly plunge-frozen in liquid ethane using an FEI Vitrobot Marked IV (Thermo Fisher Scientific). Data collection was carried out using a Titan Krios electron microscope, operated at 300 kV and equipped with a K3 direct electron detector camera situated behind a BioQuantum energy filter. A total of 13,370 (carbon layer) and 14,400 (graphene layer) dose-fractionated movies were collected, with an electron exposure of 50 electrons per $Å^2$ and a defocus range of -1.0 μm to -2.0 μm. All movies were acquired in super-resolution mode, with a pixel size of 0.525 Å.

Cryo-EM data processing

Cryo-EM data for the NRC4 resistosome was processed using CryoSPARC.[63] Initial steps included Patch Motion Correction and Patch CTF Estimation.[63] Particles were picked using Blob Picker, extracted into 100-pixel boxes, and binned by a factor of 4 to accelerate data processing. Following several rounds of 2D classification, clear top views of the NRC4 complex and two distinct side views were identified, revealing the presence of both hexameric and dodecameric NRC4 resistosome assemblies. To specifically pick particles for the hexameric or the dodecameric NRC4 resistosomes, two corresponding templates were chosen for a round of template-based picking. Particles representing the hexameric resistosome were extracted using a 90-pixel box with a pixel size of 4.2 Å. After several rounds of 2D classification, classes with clear secondary structural features were selected. This yielded 166,926 particles, which were re-extracted into 360-pixel boxes with a pixel size of 1.05 Å. An initial model was generated through Ab-initio Reconstruction with C1 symmetry. After two rounds of Heterogeneous Refinement with C1 symmetry, 80,368 particles were chosen for Non-uniform Refinement with C6 symmetry. This procedure resulted in a cryo-EM map at 2.81 Å resolution. The map was further improved through Defocus Refinement and Global CTF Refinement, resulting in a final resolution of 2.66 Å that was used for model building (Figures S2–S4).

Particles representing the dodecameric resistosome were extracted using 100-pixel boxes after binning by 4 to accelerate data processing. Multiple rounds of 2D classification were conducted to remove damaged particles or contaminants, while retaining as many "good" particles as possible, even if some exhibited lowered resolution features. 1,068,393 particles were subsequently re-extracted using a 400-pixel box and a pixel size of 1.05 Å. An initial model was constructed through Ab-Initio Reconstruction with C1 symmetry, providing an initial, low-resolution view of the double-layer resistosome. The dataset was partitioned into two subsets, each subjected to three rounds of Heterogeneous Refinement with C1 symmetry. The best classes resulting from this process were chosen and further cleaned through 2D classification. The "best" particles (28,066) displaying clear secondary structural features were selected and refined to a resolution of 3.64 Å through Non-uniform Refinement with D6 symmetry. The resolution was further improved by Defocus Refinement and Global CTF Refinement, resulting in a 3.54 Å cryo-EM map that was used for subsequent model building and structural interpretation (Figures S2–S4).

Model building and validation

The structural models of the five NRC4 protein domains, namely CC, NBD, HD1, WHD and LRR, were initially predicted using AlphaFold.[49,50] Subsequently, each domain structure was docked into the hexameric NRC4 cryo-EM map using rigid body fitting in ChimeraX.[64–66] Atomic models were manually adjusted residue by residue in COOT.[67] A similar approach was followed for the dodecameric NRC4 model assembly. In this case, AlphaFold Multimer was used to predict the dimerized structure of the α1-helix of the CC domain, which was then docked into the cryo-EM map through rigid body fitting. The resulting models were refined against the hexameric and dodecameric NRC4 cryo-EM density maps using real space refinement in PHENIX.[68] The statistics of cryo-EM data collection, processing, model building and validation are listed in Table 1. Figures were generated using ChimeraX,[64–66] PyMOL (Schrödinger) and COOT.[67]

In planta Ca^{2+} influx assay

Agrobacterium strains were syringe-infiltrated into *N. benthamiana* leaves expressing GCaMP3. After a 5-hour incubation, leaf discs with a diameter of 0.4 cm were carefully collected using a cork borer and transferred to a 96-well flat bottom black Corning assay plate containing 200 μL distilled water in each well. The plate was then kept on the bench for 1 hour to reset $[Ca^{2+}]_{cyt}$ evoked by the sampling process, followed by fluorescence recording of GCaMP3 at 45-second intervals by a Perkin-Elmer Envision multilabel plate reader. GCaMP3 emission was collected using an FITC top mirror at 535 nm with excitation light at 485 nm. The data plotted in the graphs represent the average values obtained from replicate leaf discs. For external Ca^{2+} treatment, collected leaf discs were transferred to the plate containing either distilled water or a 10 mM $CaCl_2$ solution, followed by 1 hour equilibration and Ca^{2+} recording procedure as described above. For Ca^{2+} blocker treatment, *Agrobacterium* with 2 mM $LaCl_3$ in the infiltration buffer were co-infiltrated into *N. benthamiana* leaves for the subsequent Ca^{2+} recording procedure.

Cell viability assays

HEK293FT cells were seeded at 4×10^5 cells/well in 12-well plates for transfection. The following day, the cells were transfected with plasmids encoding mCherry, NRG1.1 DV-mCherry, and NRC4 DV-mCherry using Mirus TransIT-LT1 Transfection Reagent (Mirus,

Please cite this article in press as: Liu et al., Activation of the helper NRC4 immune receptor forms a hexameric resistosome, Cell (2024), https://doi.org/10.1016/j.cell.2024.07.013

MIR2300) following the manufacturer's instructions. Individual wells were imaged over time at 10x magnification with an IncuCyte System (Sartorius) in a 37°C, 5% CO_2 incubator. Protein expression was tracked by mCherry fluorescence, and cell confluence per image was calculated using IncuCyte Analysis Software.

HEK293FT cells were plated at 2×10^4 cells/well in 96-well plates and transfected with mCherry, NRG1.1 DV-mCherry, and NRC4 DV-mCherry plasmids using Mirus TransIT-LT1 Transfection Reagent (Mirus, MIR2300). Cell viability was measured at 48 hours post-transfection using CellTiter-Glo (Promega) according to the manufacturer's instructions.

Fluorescence microscopy assay

HEK293FT cells were seeded on 8-well chamber slides and transfected with mCherry, NRG1.1 DV-mCherry, and NRC4 DV-mCherry plasmids using Mirus TransIT-LT1 Transfection Reagent (Mirus, MIR2300). Cells were fixed with 4% PFA at 48 hours post-transfection and stained with Wheat Germ Agglutinin (Alexa Fluor 488, Invitrogen) and Hoechst for 10 minutes at room temperature. Subsequently, the cells were washed with PBS and mounted using Vectashield mounting medium (Vector Laboratories, H-1000). Images were acquired with an inverted confocal microscope (Zeiss LSM 800) and processed with ZEN software (Zeiss). Image analysis was performed with the ImageJ software.

Imaging of $[Ca^{2+}]_{cyt}$ in HEK293T cells

Experiments were performed as described.[28] HEK cells were transfected with a pSBtet-Pur vector allowing for doxycycline-inducible expression of either NRC4 DV or NRG1.1 DV. Transfections were performed using lipofectamine 3000 (Invitrogen), following the manufacturer's instructions. All three constructs were YFP-tagged in C-terminal and human codon optimized. Cells were then seeded on eight-well chambered cover glasses (Nunc Lab-tek 155411) and grown overnight in a CO_2 incubator at 37°C. Expression of the chimeric proteins were induced with 1 μg mL-1 doxycycline for 6 to 8h and a Fura-2-based Ca^{2+} imaging assay was performed as previously.[28] Cells were loaded with the Ca^{2+} sensitive dye Fura-2AM (5 μM; Sigma), rinsed and incubated in a low [$CaCl^2$] standard buffer containing 130 mM NaCl, 3 mM KCl, 0.6 mM MgCl2, 10 mM glucose, 10 mM HEPES, pH7.4 (adjusted with NaOH), and 0.1 mM $CaCl^2$ for 30 min. A 7.5 mM $CaCl^2$ standard buffer was added with a peristaltic pump (Dynamax RP-1, Rainin) to adjust final [$CaCl_2$] to 2.5 mM. Fura-2 fluorescence imaging was performed using the Zeiss Axiovert 200 microscope equipped with two filter wheels (Lambda 10-3; Sutter Instruments) and a CMOS camera (Prime sCMOS; Roper Scientific). Excitation was at 340 nm and 380 nm, and emission at 510 nm. Images were collected using the MetaFluor Fluorescence Ratio Imaging Software (Molecular Devices). 10 cells per well were used for analysis.

Xenopus oocyte electrophysiology

All constructs were cloned into pGEMHE vectors using Gibson cloning. cRNAs were generated from the indicated constructs following the instruction provided by the mMESSAGE mMACHINE T7 ULTRA Transcription kit (Thermo Fisher SCIENTIFIC, Ca# AM1345), and the quality of cRNAs was confirmed using Agilent Bioanalyzer. Each oocyte was injected with 2 ng of the respective cRNA. The oocytes were incubated at 16 °C for 1 day in ND96 buffer, which contains 96 mM NaCl, 2 mM KCl, 1 mM $MgCl_2$, 1.8 mM $CaCl_2$, 10 mM HEPES/NaOH, pH 7.4. Two-electrode voltage clamp (TEVC) recordings were performed using an Axoclamp 900A amplifier and a Digidata 1550 low-noise data acquisition system (Molecular Devices). The recordings were conducted in a recording buffer containing 5 mM MES-Tris (pH 5.5), 30 mM $CaCl_2$, 1 mM KCl, 2 mM NaCl, and 130 mM mannitol. Voltage steps ranging from +40 mV to −160 mV were applied in decrements of −20 mV.

QUANTIFICATION AND STATISTICAL ANALYSIS

Statistical analyses performed using GraphPad Prism 8.0. Data for testing the significant differences were performed using One-way ANOVA.

Supplemental figures

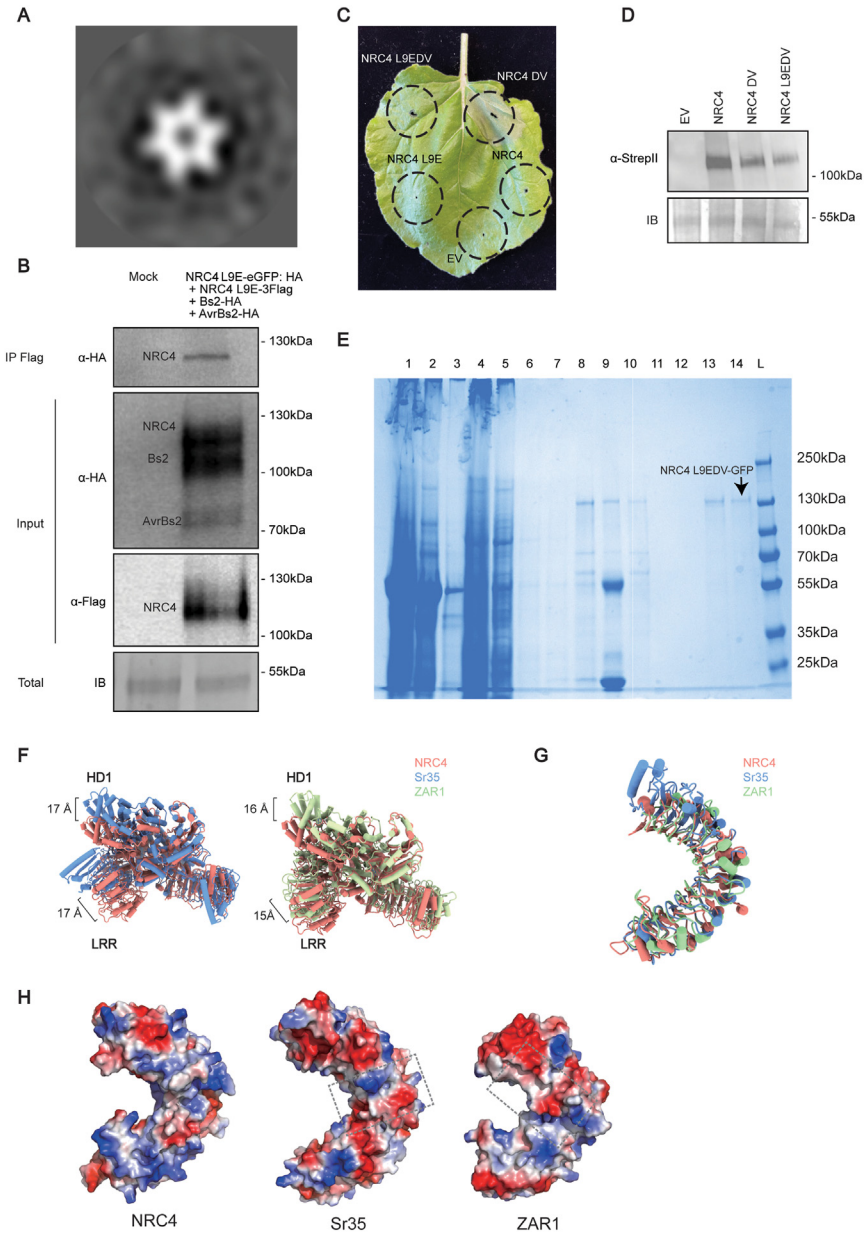

Figure S1. Comprehensive characterization of NRC4 resistosome formation, plant phenotype response, and protein purification, related to Figure 1

(A) Representative two-dimensional (2D) classification image of the hexameric NRC4 resistosome activated by the sNLR Bs2 and effector AvrBs2, as revealed by negative staining.

(B) NRC4 self-associates but does not associate with Bs2 upon AvrBs2 effector recognition. *Agrobacterium* strains harboring designated vectors were co-infiltrated into *N. benthamiana* leaves. Subsequent coIP was performed using Anti-FLAG M2 affinity beads, followed by SDS-PAGE and immunoblotting with α-FLAG or α-HA antibodies. An InstantBlue Coomassie-stained gel was used as a loading control (IB, InstantBlue; IP, immunoprecipitation).

(C) Phenotypic response of *N. benthamiana* leaves infiltrated with *Agrobacterium* carrying StrepTag II constructs, with cell death observed 2 day post-infiltration.

(D) StrepTag II proteins extracted from the leaves 2 days post-infiltration, analyzed by SDS-PAGE and western blotting with an α-StrepTag II antibody. An InstantBlue Coomassie-stained gel serves as a loading control.

(E) Purification of the NRC4 L9EDV complex, with samples analyzed by SDS-PAGE and stained with InstantBlue Coomassie.

(legend continued on next page)

(F) Structural comparison of the NRC4 resistosome with Sr35 and ZAR1 resistosomes is facilitated by displaying two adjacent protomers for clarity. The protomer on the right side of the NRC4 dimer is superimposed with Sr35 and ZAR1, revealing rearrangements in the HD1 and LRR domains of the adjacent protomer on the left. These domain rearrangements in NRC4 contribute to the formation of higher oligomeric states. Notably, the distance between two adjacent LRR domains in NRC4 is smaller than that observed in Sr35 and ZAR1.

(G) Structural alignment of LRR domains of NRC4, Sr35 (PDB:7XC2), and ZAR1 (PDB: 6J5T) in their active states.

(H) Electrostatic surface views of the LRR domains of NRC4, Sr35, and ZAR1 resistosomes. In Sr35 and ZAR1, the effector binding regions are highlighted with gray dashed boxes.

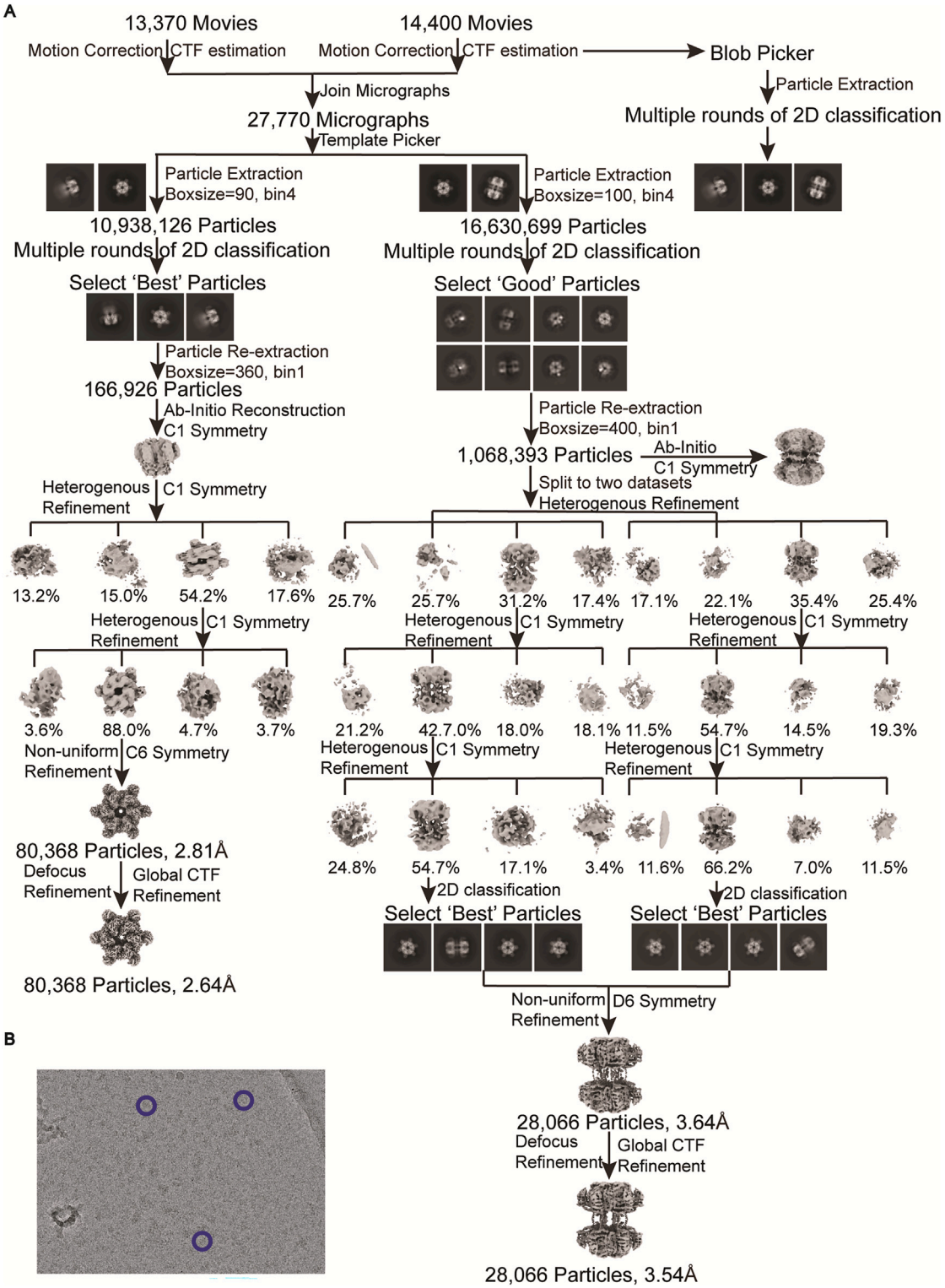

Figure S2. Cryo-EM data processing workflow, related to Figure 1

(A) Data processing workflow from the collection of movies to the reconstruction of the NRC4 resistosome.

(B) A representative cryo-EM image of the NRC4 dataset, with NRC4 particles indicated by blue circles.

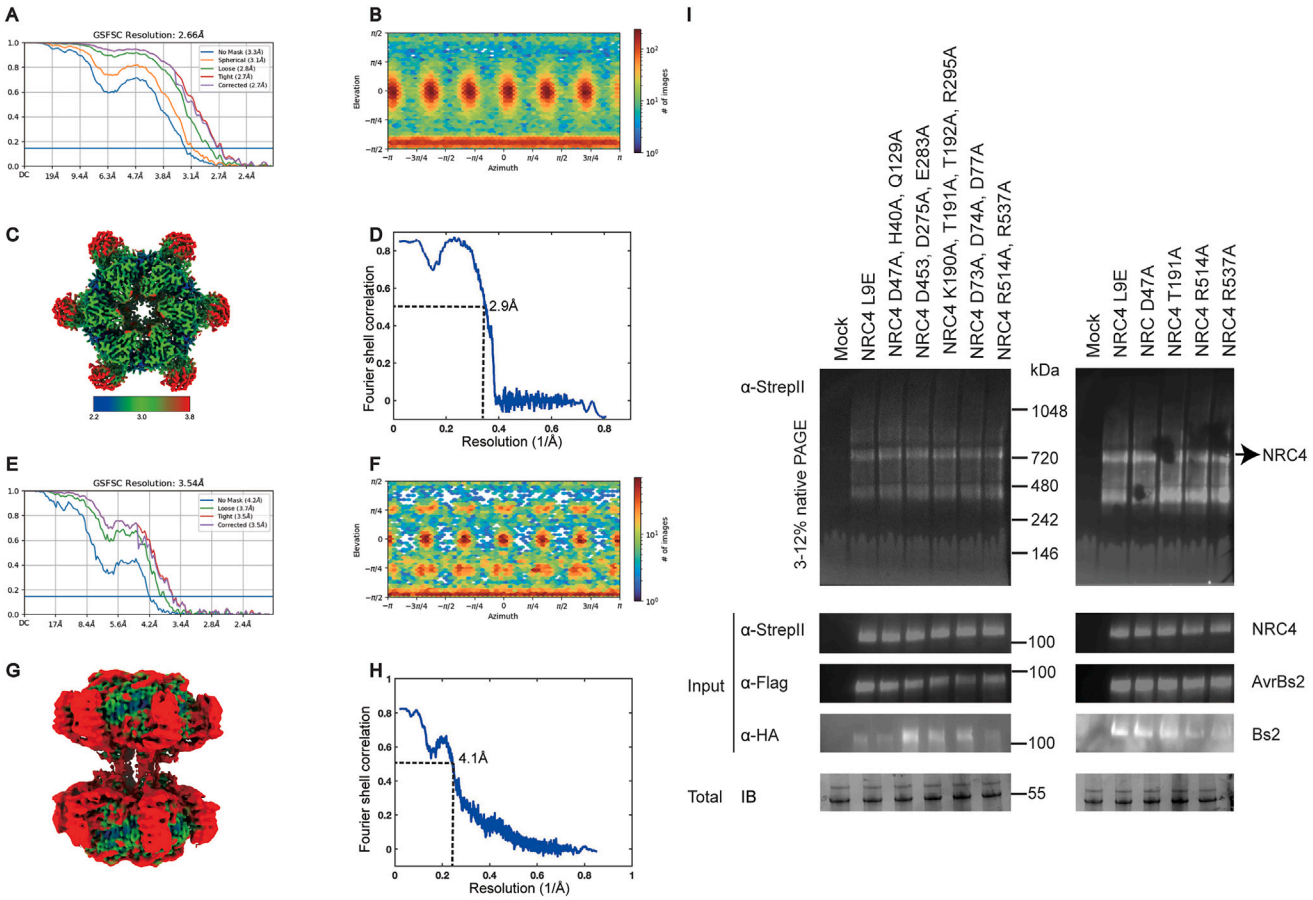

Figure S3. Map quality of the NRC4 resistosome and the oligomerization status of NRC4 mutants, related to Figure 1

(A–D) GSFSC curve, angular distribution of the final 3D reconstruction, local resolution, and model vs. map FSC plot, respectively, for the NRC4 hexamer. (E–H) GSFSC curve, angular distribution of the final 3D reconstruction, local resolution, and model vs. map FSC plot, respectively, for the NRC4 dodecamer. (I) Mutations in the residues required for HR in *N. benthamiana* still result in the oligomerization upon activation by Bs2 and AvrBs2. Total protein was extracted as described in the STAR Methods and extracts were analyzed using BN-PAGE and SDS-PAGE assays. Proteins were run on both native and denaturing PAGE in parallel and immunoblotted with the appropriate antisera labeled on the left. Approximate molecular weights (kDa) of the proteins are shown on the right. Black asterisk indicates bands corresponding to the activated NRC4 hexamer. An InstantBlue Coomassie-stained gel was used as a loading control (IB, InstantBlue).

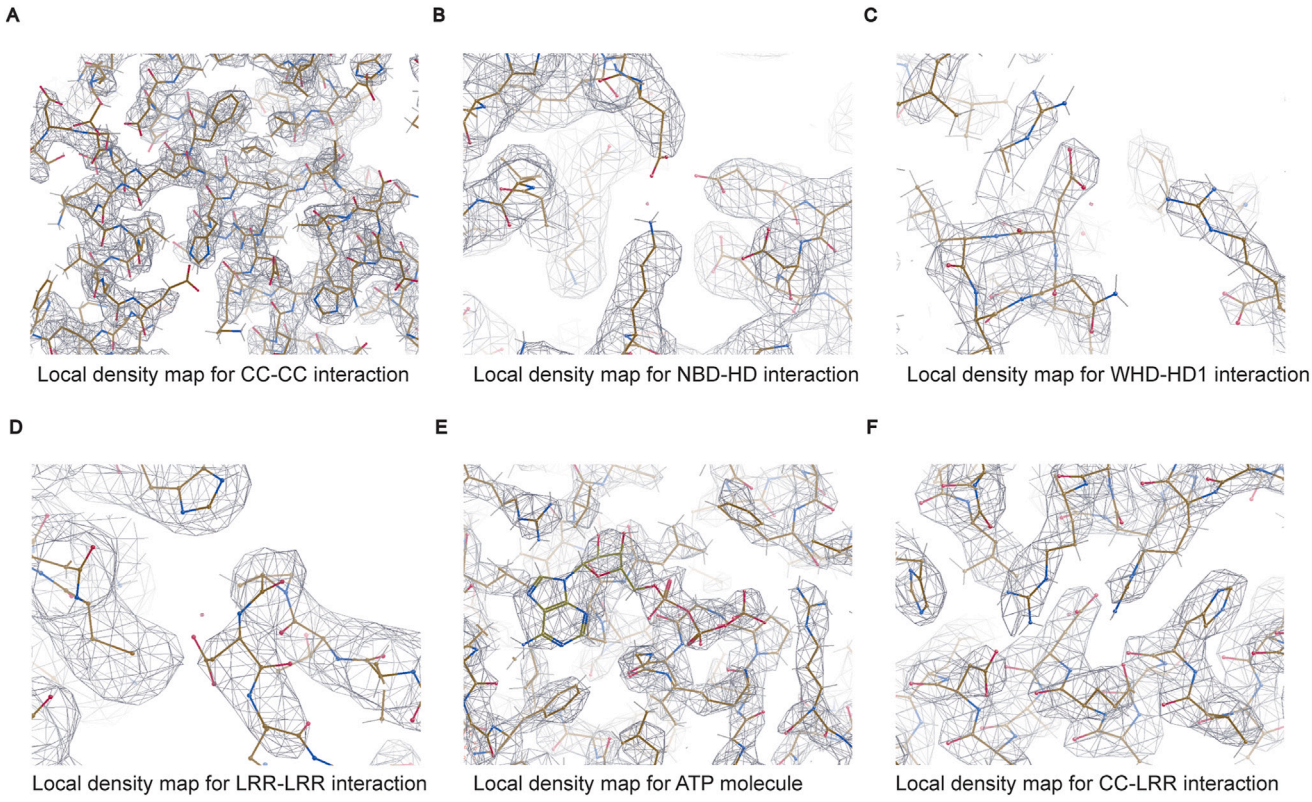

Figure S4. Local cryo-EM map densities of the NRC4 resistosome, related to Figure 2

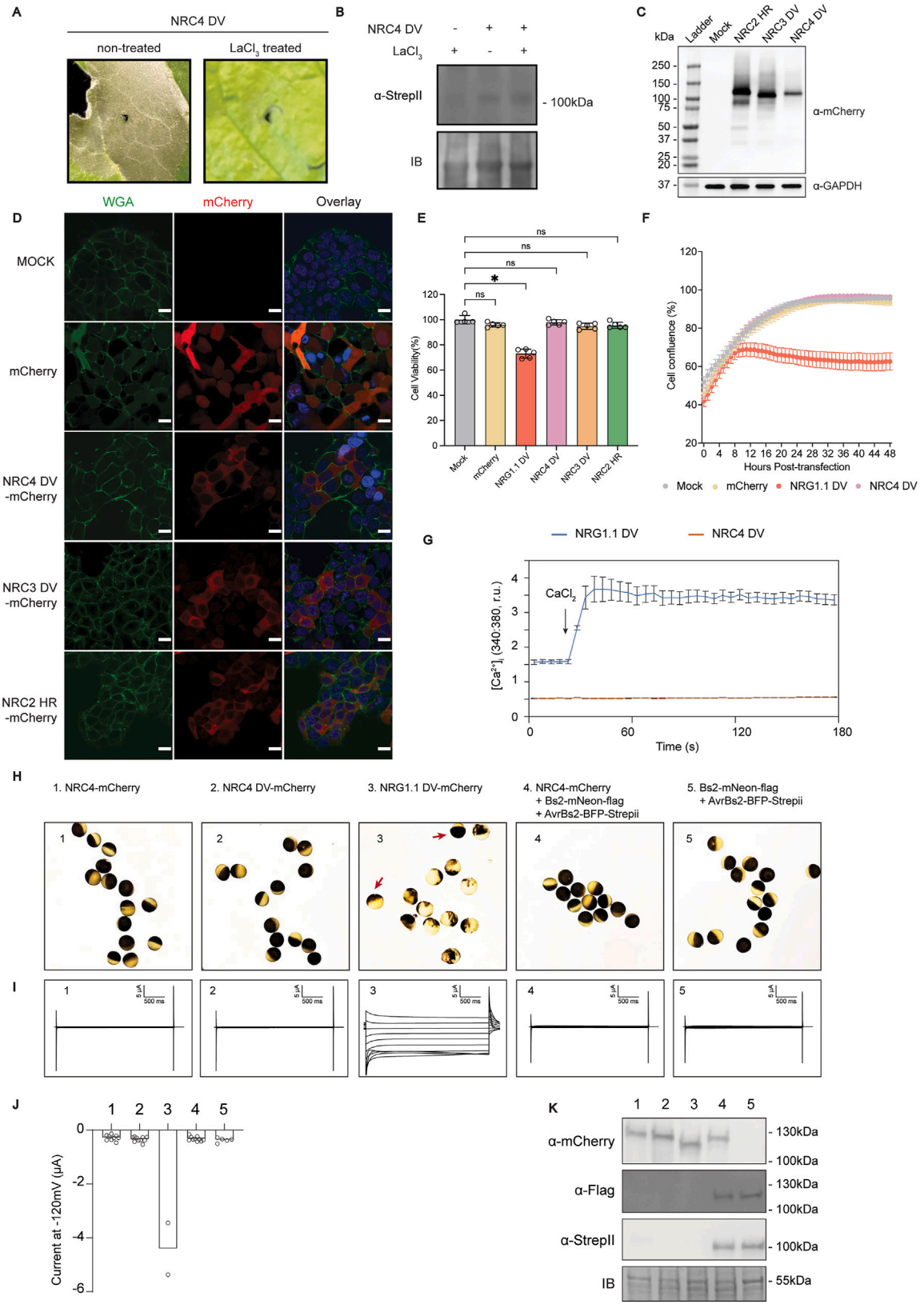

(legend on next page)

Figure S5. $LaCl_3$ mitigates NRC4 DV-mediated cell death in *N. benthamiana* leaves but not in animal cells, related to Figure 4

(A) HR phenotypes of *N. benthamiana* leaves upon the expression of the activation mimic NRC4 DV in the absence and presence of the Ca^{2+} channel blocker $LaCl_3$ (2 mM).

(B) Protein expression levels of NRC4 DV in *N.benthamiana* leaves were evaluated using SDS-PAGE and subsequent immunoblotting with α-StrepTag II antibody. An InstantBlue Coomassie-stained gel was used as a loading control.

(C) Protein expression levels of the activation mimics NRC2 HR, NRC3 DV, and NRC4 DV in HEK293 cells were evaluated using SDS-PAGE and subsequent immunoblotting with α-mCherry antibody. α-GAPDH was used as a loading control.

(D) Confocal imaging of mock, mCherry, NRC4 DV-mCherry, NRC3 DV-mCherry, and NRC2 HR-mCherry transfected HEK293 cells at 48 h post-transfection. The mCherry signal is shown in red, wheat germ agglutinin (WGA) staining in green, and Hoechst nuclear stain in blue. Scale bars represent 20 μm.

(E) Cell viability of mock, mCherry, NRG1.1 DV-mCherry, NRC2 HR-mCherry, NRC3 DV-mCherry, and NRC4 DV-mCherry transfected HEK293 cells at 48 h post-transfection, as measured using the CellTiter-Glo luminescent cell viability assay. Data are presented as mean values ± SD, $n = 4$ or 5 biologically independent samples, one-way ANOVA with Dunnett multiple comparison test, $p < 0.01$(*), $p > 0.01$ (ns).

(F) Time course of cell confluence for mock, mCherry, NRG1.1 DV-mCherry, and NRC4 DV-mCherry transfected HEK293 cells.

(G) Ratiometric measurements of $[Ca^{2+}]_{cyt}$ in HEK293 cells expressing YFP-tagged activation mimic NRG1.1 DV or NRC4 DV. Cells were incubated in a low Ca^{2+} buffer before $CaCl_2$ addition (black arrow). Fluorescence pictures (at excitation 340 and 380 nm) were taken every 5 s for 3 min.

(H) The activation mimic NRC4 DV does not induce cell death or exhibit Ca^{2+} channel activity in *Xenopus* oocytes. Injected oocytes were photographed 24 h post-injection. The red arrow points to oocytes that remained viable after the injection of NRG1.1 DV cRNA.

(I) Typical TEVC recording.

(J) Current amplitudes at −120 mV of inward currents in *Xenopus* oocytes.

(K) Protein expression levels in *Xenopus* oocytes cells were evaluated using SDS-PAGE and subsequent immunoblotting with α-mCherry, α-FLAG, and α-StrepTag II antibodies. Coomassie-stained gel was used as a loading control (IB, InstantBlue). (1): NRC4-mCherry-myc; (2): NRC4 DV-mCherry-myc; (3): NRG1.1 DV-mCherry-myc; (4): NRC4-mCherry-myc, Bs2-mNeon-FLAG, and AvrBs2-BFP-StrepTag II; (5): Bs2-mNeon and AvrBs2-BFP-StrepTag II.

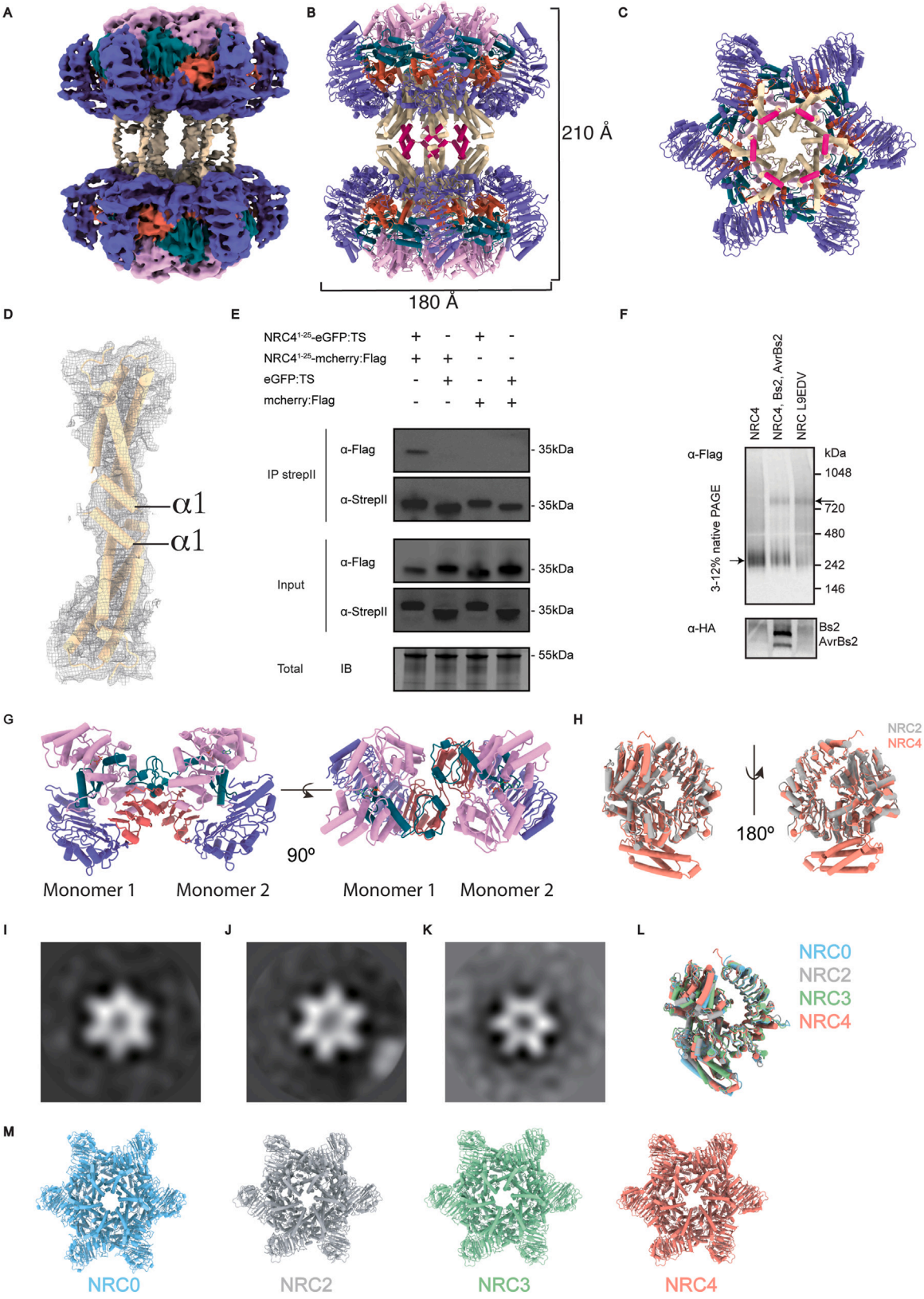

(legend on next page)

Figure S6. Dodecameric and dimeric configuration of NRC4, and structural comparisons with other NRCs, related to Figure 6

(A–C) (A) Cryo-EM density map of the dodecameric NRC4 resistosome, (B) corresponding atomic model, and (C) cross-sectional of the dodecameric structural model. Twelve NRC4 protomers form a dumbbell-shaped structure, measuring ~180 Å in diameter and 210 Å in height. The α1 helices in the CC domains, which bridge the formation of the double-layer structure, are highlighted in pink.

(D) Cryo-EM map of the two CC domains originating from adjacent protomers, situated on opposite sides of the double-layer hexamer. The CC domains play a crucial role in mediating the formation of the dodecameric NRC4 resistosome, where the α1-helices interact with their counterparts from the opposite side.

(E) The co-immunoprecipitation (coIP) assay confirming the interaction between the two α1 helices (1–25). *Agrobacterium* strains harboring designated vectors were co-infiltrated into *N. benthamiana* leaves. Subsequent coIP experiments utilized Strep-Tactin XT 4Flow high-capacity resin for protein extraction, followed by analysis through protein gel blotting with α-FLAG or α-StrepTag II antibodies. An InstantBlue Coomassie-stained gel was used as a loading control (IB, InstantBlue; IP, immunoprecipitation).

(F) Oligomeric states of FLAG-tagged NRC4 were verified through BN-PAGE immunoblotting in *N. benthamiana*. The approximate molecular weights (in kDa) of the proteins are shown on the right. Black arrows indicate signals corresponding to the molecular weights of the homodimer or hexamer. HA tagged Bs2 and AvrBs2 were detected by western blot in the lower panel.

(G) The structural model of the wild-type NRC4 was predicted using SWISS-MODEL, with the NRC2 homodimer structure (PDB: 8RFH) serving as the template.

(H) Structural comparison of the NRC4 monomer with the inactive NRC2 structure (PDB: 8RFH). The monomeric structure of NRC4 is predicted by AlphaFold and aligned to one copy of the NRC2 dimer. The RMSD between these two proteins is 1.052. NRC4 is colored in orchid, ZAR1 in light green, and NRC2 in gray.

(I–K) Examples of 2D class averages obtained from negative staining of active NRC0, NRC2, and NRC3, respectively. All of these active forms of NLRs displayed a hexameric conformation.

(L) Structural comparison of the protomers of active NRC0, NRC2, NRC3, and NRC4 proteins. The structures of NRC0, NRC2, and NRC3 were predicted by SWISS-MODEL.

(M) Structural comparison of modeled active NRC0, NRC2, and NRC3 structures with NRC4. The homologous structures of NRC0, NRC2, and NRC3 were predicted by SWISS-MODEL and then rigidly fitted into the NRC4 map.